Loss of genome maintenance accelerates podocyte damage and aging

Fabian Braun[1,2,3+*], Amrei M. Mandel[1,4,5+], Linda Blomberg[1,4], Milagros N. Wong[2,3], Georgia Chatzinikolaou[6], Viji Nair[7], Roman Akbar-Haase[1,4], Victor G. Puelles[2,3], David H. Meyer[4,20], Phillip J. McCown[7], Fabian Haas[2,3], Mahdieh Rahmatollahi[1,4], Damian Fermin[9], Gisela G. Slaats[1,4], Tillmann Bork[10], Christoph Schell[10,11], Sybille Koehler[1,2,3], Paul T. Brinkoetter[1,4], Maja T. Lindenmeyer[2,3], Clemens D. Cohen[3,12], Martin Kann[1,4], Wilhelm Bloch[13], Matthew G. Sampson[14,15,16], Martijn ET Dollé[17], Matthias Kretzler[7], George A. Garinis[6,18], Tobias B. Huber[2,3], Bernhard Schermer[1,4,19], Thomas Benzing[1,4,19], Björn Schumacher[3,18,20], and Christine E. Kurschat[1,4*]

[1]Department II of Internal Medicine and Center for Molecular Medicine Cologne, University of Cologne, Faculty of Medicine and University Hospital Cologne, Cologne, Germany
[2]III. Department of Medicine, University Medical Center Hamburg-Eppendorf, Hamburg, Germany
[3]Hamburg Center for Kidney Health (HCKH), University Medical Center Hamburg-Eppendorf, Hamburg, Germany
[4]Cologne Excellence Cluster on Cellular Stress Responses in Aging-Associated Diseases (CECAD), University of Cologne, Faculty of Medicine and University Hospital Cologne, Cologne, Germany
[5]Research Center On Rare Kidney Diseases (RECORD), University Hospital Erlangen, Erlangen, Germany
[6]Institute of Molecular Biology and Biotechnology, Foundation for Research and Technology-Hellas, Heraklion, Crete, Greece.
[7]Division of Nephrology, Department of Internal Medicine, University of Michigan, Ann Arbor, Michigan, USA.
[8] Department of Clinical Medicine, Aarhus University, Aarhus, Denmark
[9]Department of Pediatrics-Nephrology, University of Michigan, Ann Arbor, Michigan
[10]Department of Medicine IV, Faculty of Medicine, University of Freiburg, Freiburg, Germany.
[11]Institute of Surgical Pathology, Faculty of Medicine, University of Freiburg, Freiburg, Germany.
[12]Nephrological Center, Medical Clinic and Polyclinic IV, University of Munich, Munich, Germany
[13]Department of Molecular and Cellular Sport Medicine, German Sport University Cologne, Cologne, Germany
[14]Division of Nephrology, Boston Children's Hospital, Boston, Massachusetts, USA
[15]Harvard Medical School, Boston Massachusetts, USA
[16]Broad Institute, Cambridge, Massachusetts, USA
[17]National Institute for Public Health and the Environment, Bilthoven, The Netherlands.
[18]Department of Biology, University of Crete, Heraklion, Crete, Greece.
[19]Systems Biology of Ageing Cologne, SyBaCol, University of Cologne, Germany
[20]Institute for Genome Stability in Aging and Disease, Medical Faculty, University of Cologne, Germany
+ indicates equal contribution

Correspondence should be addressed to:

Christine E. Kurschat
Nephrology Research Lab
CECAD
University of Cologne
Joseph Stelzmann-Straße 26
50931 Cologne, Germany

Tel +49-221-478 4480
Fax +49-221-478 5959
E-mail: christine.kurschat@uk-koeln.de

Fabian Braun
E-mail: fa.braun@uke.de
Twitter: @fab_braun

Abstract:

DNA repair is essential for preserving genome integrity and ensuring cellular functionality and survival. Podocytes, post-mitotic glomerular epithelial cells, bear limited regenerative capacity, and their survival is indispensable to maintain the function of the kidney's filtration units. While podocyte depletion is a hallmark of the aging process and of many proteinuric kidney diseases, the underlying factors remain unclear.

We investigated DNA repair in podocyte diseases by using a constitutive and an inducible podocyte-specific knockout mouse model for *Ercc1,* a multifunctional endonuclease cofactor involved in nucleotide excision repair (NER), interstrand crosslink (ICL) repair, and DNA double-strand break (DSB) repair. We assessed the consequences of *Ercc1* loss *in vivo,* complemented by mechanistical *in vitro* studies of induced DNA damage in cultured podocytes. Furthermore, we characterized DNA damage-related alterations in mouse and human renal tissue of different ages as well as in patient biopsies with minimal change disease and focal segmental glomerulosclerosis.

Podocyte-specific *Ercc1* knockout resulted in accumulation of DNA damage with ensuing proteinuria, podocyte loss, glomerulosclerosis, renal insufficiency, and reduced lifespan. The response to genomic stress was different to the pattern reported in other cell types, as podocytes activated mTORC1 signaling upon DNA damage *in vitro* and *in vivo*. The induced mTORC1 activation was abrogated by inhibiting DNA damage response through DNA-PK and ATM kinases *in vitro*. Moreover, pharmacological inhibition of mTORC1 modulated the development of glomerulosclerosis in *Ercc1*-deficient mice. Perturbed DNA repair gene expression and genomic stress was also detected in podocytes of human focal segmental glomerulosclerosis, characterized by podocyte loss. Beyond that, DNA damage accumulation occurred in podocytes of healthy aging mice and humans.

These findings reveal that genome maintenance is crucial for podocyte maintenance, linked to the mTORC1 pathway, and involved in the aging process as well as in the development of glomerulosclerosis, potentially serving as a therapeutic target in the future.

Keywords:

Podocyte, DNA Damage, Aging, Ercc1, mTORC1, glomerulosclerosis

90 **Introduction:**

91 Most cells of the body are constantly subjected to various DNA damaging agents (1, 2). Therefore,
92 cells depend on numerous DNA repair mechanisms to counteract transcription stress (3).
93 Mutations in DNA repair genes result in a variety of pathologies ranging from cancer to progeroid
94 syndromes (4, 5). The specific importance of genome maintenance in cells with limited
95 regenerative capacity is demonstrated by the prevalence of neurodegeneration as a hallmark of
96 DNA repair deficiency syndromes (6).

97 Glomerular podocytes are terminally differentiated, post-mitotic cells with little to no replacement
98 capacity post-development (7). As an integral part of the primary filtration unit of the kidney (8),
99 podocyte depletion is a leading cause of chronic kidney disease due to diabetes, hypertension,
100 and other glomerulopathies, with ensuing loss of protein into the urine (9) and progressive renal
101 insufficiency. A milder phenotype without overt proteinuria is present in aged kidneys, with globally
102 sclerosed glomeruli due to decreasing numbers of podocytes with age (10). The precise
103 pathomechanisms leading to podocyte depletion, however, are incompletely understood.
104 Protecting this finite number of cells is, therefore, an important therapeutic goal (11).

105 Lately, first studies have indicated the importance of genome maintenance for renal health (12,
106 13). Mutations in the kinase endopeptidase and other proteins of small size (KEOPS) complex
107 genes caused proteinuria and induced DNA damage response (DDR) *in vitro* (14). Likewise,
108 glomerular DNA damage was found to be associated with declining kidney function (15) and cells
109 isolated from the urine of patients suffering from diabetes and hypertension showed increased
110 levels of DNA strand breaks (16). Furthermore, the glomeruli of a progeric mouse model were
111 identified to share the expression profile of aged glomeruli, indicating a role of DNA damage repair
112 in glomerular aging (17).

113 Several studies have proposed an interplay between DNA damage signaling and the mechanistic
114 target of rapamycin (mTOR) pathway with factors induced by DNA damage exhibiting repressive
115 effects on mTOR-complex1 (mTORC1) (18–20) and increased mTORC1 activity leading to
116 transcription stress (21–23). This is of particular interest for podocytes, as they are highly
117 dependent on a rigorous control of mTOR activity. While mTORC1-driven hypertrophy is a
118 protective response upon podocyte depletion (10, 24, 25), mTORC1 overactivation drives
119 pathologic hyperproliferation and sclerosis (26, 27). In line with these findings, side effects of
120 pharmacological mTORC1 inhibition entail proteinuria and glomerular scarring (28–34).

121 Our group has proposed a role of DNA damage in glomerular aging by investigating glomeruli of
122 the progeric *Ercc1* -/delta mouse (17). We followed up on these analyses and detected a newly

123 discovered hallmark of aging – the shift towards transcription of smaller RNAs resulting from
124 transcriptional stalling (35). To further address the involvement of podocytes in the process of
125 accelerated aging, we created a podocyte-specific *Ercc1* knockout mouse model. Podocyte-
126 specific DNA damage accumulation resulted in proteinuria, podocyte loss, glomerulosclerosis, and
127 renal insufficiency in mice. Strikingly, both *in vivo* and *in vitro* analyses revealed mTORC1
128 activation upon DNA damage, indicating a cell type-specific response. Inhibiting DNA damage
129 response through DNA-PK and ATM inhibition diminished mTORC1 activation. In turn, inhibiting
130 mTORC1 activation moderately improved the glomerulosclerotic phenotypes in two Ercc1-
131 deficient mouse models. In both humans and mice DNA damage foci were increased in podocyte
132 nuclei of aged healthy kidneys accompanying mTORC1 activation. Ancillary, we identified
133 perturbations in the expression of DNA repair genes in glomeruli and podocytes from human
134 glomerular diseases associated with podocyte depletion and observed a significant increase of
135 DNA damage in podocytes of patients suffering from focal segmental glomerulosclerosis. These
136 results directly link genome maintenance to glomerular diseases and identify DNA damage
137 accumulation as a hallmark of human podocyte aging.
138
139 **Methods:**
140 *GSEA Analysis*
141 Raw data were downloaded from GSE43061, normalized with RMA (36), and further processed
142 with limma (37). The log fold-changes of the comparison Ercc1 14 weeks vs. WT 14 weeks were
143 used as input for the gene length GSEA analysis (17). The p-values and adjusted p-values are
144 depicted in the plots. The enrichment analysis for chromosomal gene distributions was done in R
145 v3.6.3 with the GSEA function of clusterProfiler (38), v3.14.3 was used with maxGSSize=6000
146 and nPerm=20000.
147 *Mice*
148 Mice were bred in a mixed FVB/CD1 (*Ercc1* pko) or FVB/CD1/C57BL/6 (*Ercc1* ipko) background.
149 All offspring was born in normal mendelian ratios. Mice were housed in the animal facility of the
150 Center for Molecular Medicine Cologne or the Cluster of Excellence – Cellular Stress Responses
151 in Aging-Associated Diseases. Following federal regulations, the Animal Care Committee of the
152 University of Cologne reviewed and approved the experimental protocols. Animals were housed
153 at specific pathogen-free (SPF) conditions with three-monthly monitoring according to FELASA
154 suggestions. Housing was done in groups of less than six adult animals receiving CRM pelleted
155 breeder and maintenance diet irradiated with 25 kGy (Special Diet Services, Witham, UK) and

156 water *ad libitum*. Spot urine was collected once a week during cage changes or during sacrifice.
157 Tamoxifen was administered at 400 mg/kg Tamoxifen in dry chow.
158 For rapamycin injection studies male and female *Ercc1*$^{fl/fl}$ (ctrl) and *Ercc1*; *Nphs2.Cre* (pko) mice
159 at week 6 of age were injected intraperitoneally 3 times/week with 2 mg/kg bodyweight of
160 rapamycin diluted in 5% ethanol, 5% tween 80, and 5% PEG 400 or with 5% ethanol, 5% tween
161 80, and 5% PEG 400 as vehicle. Urine collection was performed 2 times/week and mice were
162 sacrificed at week 13 of age for serum and kidney tissue isolation. All animals were maintained in
163 grouped cages on a 12h light/dark cycle. Mice were kept on a regular diet and had access to water
164 *ad libitum*. Body weight was measured weekly. Animals were housed in a temperature-controlled,
165 pathogen-free animal facility at the Institute of Molecular Biology and Biotechnology (IMBB), which
166 operates in compliance with the "Animal Welfare Act" of the Greek government, using the "Guide
167 for the Care and Use of Laboratory Animals" as its standard.
168 Mice were anaesthetized by intraperitoneal injection of 10 μl per g bodyweight of 0.01% xylocaine
169 and 12.5 mg/ml ketamine – blood was drawn from the left ventricle into a syringe rinsed with
170 Heparin sulfate and animals were perfused with cold phosphate buffered saline (PBS). Kidneys
171 were excised and embedded in OCT (Sakura, Torrance, CA) and frozen at -80°C or fixed in 4%
172 neutral buffered formalin and subsequently embedded in paraffin.
173 Archival tissue of podocyte specific *Tsc*1 knockout mice was provided by Tillman Bork (University
174 of Freiburg, Germany). *Tsc1*$^{fl/fl}$ mice were crossbred with Nphs2-Cre^{+}. For further details see ref
175 (39).
176 Tissue of *Ercc1* -/delta mice was provided by Martin Dollé (National Institute of Public Health and
177 the Environment Bilthoven, Netherlands). Further details provided in ref (40).
178 *Electron Microscopy*
179 Mice were perfused with 4% paraformaldehyde and 2% glutaraldehyde in 0.1 M sodium
180 cacodylate, pH 7.4. Postfixation was performed in the same buffer for two additional weeks at 4°C.
181 Tissue was osmicated with 1% OsO4 in 0.1 M cacodylate and dehydrated in increasing ethanol
182 concentrations. Upon infiltration and flat embedding were performed following standard
183 procedures. Toluidine blue was used to stain semithin sections of 0.5 μm. 30 nm-thick sections
184 were cut with an Ultracut UCT ultramicrotome (Reichert) and stained with 1% aqueous uranylic
185 acetate and lead citrate. Samples were studied with Zeiss EM 902 and Zeiss EM 109 electron
186 microscopes (Zeiss, Oberkochen, Germany).
187 *Podocyte isolation*

188 To isolate primary podocytes, *Ercc1*$^{fl/fl}$ mice heterozygous for the *R26mTmG* and *Nphs2.Cre*
189 transgene were sacrificed and kidneys were used for glomerular preparation, as previously
190 described (41). The glomeruli were digested and the single-cell suspension was used for
191 fluorescence-activated cell sorting.

192 *qPCR Analysis*

193 Total ribonucleic acid (RNA) was extracted from podocytes of *Ercc1/Nphs2.Cre/mTmG* mice using
194 Direct-zol™ RNA MiniPrep Kit (cat. no. R2052, Zymo Research). Isolation of glomeruli,
195 preparation of a glomerular single-cell suspension, and fluorescence-activated cell sorting was
196 done as previously described (7). Podocytes were sorted into TriReagent (cat. no. 93289, Sigma-
197 Aldrich). The complementary deoxyribonucleic acid (cDNA) was synthesized with High Capacity
198 cDNA Reverse Transcription Kit (cat. no. 4368814, Applied Biosystems). PCR was performed
199 using TaqMan™ Gene Expression Master Mix (cat. no. 4369016, Applied Biosystems) and the
200 Applied Biosystems Real-time PCR system. Real-time PCR was measured with triplicates in each
201 gene target. The sequence of the PCR primer used for *Ercc1* was: 5′-
202 AGCCAGACCCTGAAAACAG-3′ and 5′- CACCTCACCGAATTCCCA-3′ in PrimeTime Mini qPCR
203 Assay for *Ercc1* (Assay-ID: Mm.PT.58.42152282, IDT). The gene expression was calculated using
204 comparative cycle threshold method and normalized to RNA polymerase II subunit A (*Polr2a*).
205 The relative fold change of *Ercc1* expression in knockout mice was compared with WT and
206 heterozygous mice.

207 *Urinary Albumin ELISA & Creatinine measurement*

208 Urinary albumin levels were measured with a mouse albumin ELISA kit (mouse albumin ELISA
209 kit; Bethyl Labs, Montgomery, TX, USA). Urinary creatinine kit (Cayman Chemical, Ann Arbor, MI,
210 USA) was used to determine corresponding urinary creatinine values. For Coomassie Blue
211 detection of albuminuria, spot urine of mice was diluted 1:20 in 1x Laemmli buffer and urinary
212 proteins separated using poly-acrylamide gel electrophoresis with subsequent Coomassie gel
213 stain.

214 *Plasma Creatinine and Urea measurement*

215 Blood samples were centrifuged at 400 g 4°C for 20 minutes and plasma samples subsequently
216 stored at -20°C until further analysis. Creatinine and Urea were measured using standard clinical
217 protocols by the Department of Clinical Chemistry of the University of Cologne.

218 *Histologic analysis*

219 To assess morphological changes in light microscopy we performed Periodic Acid Schiff staining.
220 For specific antibody stainings, sections were deparaffinized in Xylene (VWR, Darmstadt,

221 Germany), rehydrated in decreasing concentrations of ethanol, and subjected to heat-induced
222 antigen retrieval in 10 mM Citrate Buffer pH 6 for 15 minutes. Peroxidase blocking was performed
223 in methanol mixed with 3% hydrogen peroxidase (Roth, Karlsruhe, Germany) followed by
224 Avidin/Biotin blocking (Vector, Burlingame, CA, USA) for 15 minutes each. After incubation in
225 primary antibody (anti-phospho-S6 Ribosomal Protein (Ser235/236) # 4858 – Cell Signaling
226 Technology) 1:200 in TBS 1% BSA at 4°C overnight, sections were washed in TBS and incubated
227 in biotinylated secondary antibody (Jackson Immunoresearch, West Grove, USA) 1h at room
228 temperature. For signal amplification the ABC Kit (Vector, Burlingame, CA, USA) was used before
229 applying 3,30-diaminobenzamidine (Sigma-Aldrich, St Louis, USA) as a chromogen. Hematoxylin
230 was used for counterstaining. After dehydration, slides were covered in Histomount (National
231 Diagnostics, Atlanta, USA).
232 *Immunofluorescence Staining*
233 Paraffin embedded tissue was cut into 3 μm thick sections and processed according to published
234 protocols (42). Primary antibodies (anti-γH2A.X #2577s – Cell Signalling Technology, anti-nephrin
235 #GP-N2 – Progen, anti-synaptopodin #65294 – Progen, anti-Dach1 #HPA012672 – Sigma Aldrich
236 (43), anti-phospho-S6 Ribosomal Protein (Ser235/236) # 4858 – Cell Signaling Technology), and
237 anti-p53 (anti-p53 #p53-protein-cm5 Leica Biosystems) were used at 1:200 dilution. Far-red
238 fluorescent DNA dye Draq 5 was used as a nuclear marker.
239 Cells were processed according to published protocols (44).
240 For γH2A.X foci quantification, a custom-built FIJI macro was used. In brief, podocyte nuclei were
241 identified through surrounding synaptopodin staining, segmented using the freehand tool and split
242 into single channels. Draq 5 channel was converted into binary image using auto threshold "otsu
243 dark" with subsequent particle measurement (range 5-infinite) to determine nuclear area. γH2A.X
244 channel was converted into binary image using auto threshold "MaxEntropy dark" with subsequent
245 particle measurement (range 0.02-infinite) to determine foci number and area.
246 *In vitro Experiments*
247 Conditional immortalized murine podocytes were a gift by Stuart Shankland. Cells were cultured
248 as previously described (45). Briefly, immortalized podocytes were cultured in RPMI media
249 supplemented with 10% FBS and IFNγ (Sigma-Aldrich, Taufkirchen, Germany). Cells proliferated
250 at 33°C on Primaria plastic plates (BD Biosciences, San Jose, CA, USA) until they reached a
251 confluence of 60-70%. Differentiation of podocytes was induced by seeding the cells at 37°C in
252 the absence of IFNy. After 10 days of differentiation, cells were treated with 5 or 10 μg/ml
253 Mitomycin C (#M0503 - Sigma-Aldrich, Taufkirchen, Germany) for 2h in serum-free medium,

254 followed by one washing step with PBS and another 6h incubation in serum-free medium without
255 Mitomycin C before further processing. The absence of mycoplasm infection was tested regularly
256 using the mycoplasm detection kit from Minerva biolabs (Minerva Biolabs, Berlin, Germany). For
257 experiments with DNA damage response inhibitors, differentiated cells were pre-treated with 3 μM
258 KU60019 (Selleckchem, Houston, TX, USA) or 1 μM Nedisertib (Selleckchem, Houston, TX, USA)
259 for 1 h before inducing DNA damage by UV-C or Mitomycin C treatment. Inhibitors were added
260 again after medium change following DNA damage induction to further incubate cells for 6 h before
261 cell lysis.

262 *Western Blot analysis*

263 SDS-PAGE was used for protein size separation with subsequent blotting onto polyvinylidene
264 difluoride membranes and visualized with enhanced chemiluminescence after incubation of the
265 blots with corresponding antibodies (Phospho-Histone H2A.X (Ser139); Phospho-S6 Ribosomal
266 Protein (Ser235/236) (D57.2.2E); S6 Ribosomal Protein (5G10) – Cell Signaling Technology;
267 alpha Actin – Developmental Studies Hybridoma Bank; beta-Tubulin (E7) - Developmental Studies
268 Hybridoma Bank).

269 *ERCB Human microarray analysis*

270 167 genes involved in DNA repair and nucleotide excision repair were compiled from the hallmark
271 gene set “DNA-Repair” from the Molecular Signatures Database (MSigDB) Collection (46) and
272 upon literature research. Human kidney biopsies and Affymetrix microarray expression data were
273 obtained within the framework of the European Renal cDNA Bank - Kröner-Fresenius Biopsy Bank
274 (47). Diagnostic biopsies were obtained from patients after informed consent and with approval of
275 the local ethics committees. Following renal biopsy, the tissue was transferred to RNase inhibitor
276 and micro-dissected into glomeruli and tubulo-interstitium. Total RNA was isolated, reverse
277 transcribed, and amplified as previously reported (48). Fragmentation, hybridization, staining, and
278 imaging were performed according to the Affymetrix Expression Analysis Technical Manual
279 (Affymetrix, Santa Clara, CA, USA). Published datasets of glomerular samples were analysed for
280 mRNA expression levels. Analysis included datasets from patients with minimal change disease
281 (MCD; n=14), focal segmental glomerulosclerosis (FSGS; n=23), membranous nephropathy
282 (MGN; n=21), IgA nephropathy (Glom; n=27), and hypertensive nephropathy (HTN; n=15) as well
283 as controls (living donors (LD); n=42) (GSE99340, LD data from: GSE32591, GSE37463). CEL
284 file normalization was performed with the Robust Multichip Average method using RMAExpress
285 (Version 1.0.5) and the human Entrez-Gene custom CDF annotation from Brain Array version 18
286 (http://brainarray.mbni.med.umich.edu/Brainarray/default.asp). To identify differentially expressed

287 genes, the SAM (Significance Analysis of Microarrays) method (49) was applied using SAM
288 function in Multiple Experiment Viewer (TiGR MeV, Version 4.9). A q-value below 5% was
289 considered to be statistically significant. The resulting gene expression list was censored for
290 genes, whose products were detected in a transcriptomic and proteomic analysis of wild-type
291 murine podocytes (41).

292 *Single nucleus sequencing*

293 Nuclei were prepared from kidney biopsy cores stored in RNAlater from FSGS patients enrolled
294 in the NEPTUNE study (50). The processing followed the protocol developed from the Kidney
295 Precision Medicine Project. Nuclei preparations were processed and sequenced using 10x
296 Genomics single cell sequencer. Analyses were performed on the output data files from
297 CellRanger v6.0.0 using the Seurat R package (version 3.2 and 4.0; https://cran.r-
298 project.org/web/packages/Seurat/index.html). To limit low quality nuclei and/or multiplets, we set
299 gene counts and cutoffs to between 500 and 5000 genes and examined nuclei with a mitochondrial
300 gene content of less than 10%. Nuclei were merged into a Seurat object using the CCA integrate
301 function and nuclear cluster annotation was determined by finding enriched genes in each cell
302 cluster. A comparison of these cluster selective gene profiles was compared against previously
303 identified cell marker gene sets from human kidney samples from KPMP and other sources (50).

304 *Expression quantitative trait locus (eQTL) analysis*

305 For the subgroup analysis of FSGS cohort, the procedure described in Gillies et al., 2018 was
306 used with the following exceptions: only FSGS patients were analysed (N=87) and only RNAseq
307 expression data for glomerular samples were utilized. Briefly, cis-eQTLs were identified using
308 MatrixEQTL from among variants that were located either within the annotated boundaries of a
309 gene or its surrounding region (+/- 500 kb) (51). We then adjusted for age, sex, principal
310 components of genetic ancestry, and the first 5 PEER factors (52). The genetic ancestry was
311 calculated using LD-pruned WGS data from across all 87 patients using the EPACTS tool
312 (https://genome.sph.umich.edu/wiki/EPACTS). The gene-level FDR for the MatrixEQTL was
313 controlled using TORUS. Fine mapping of the eQTLs was performed using the DAP algorithm
314 (53).

315 *Study approval*

316 All investigations involving human specimen have been conducted according to the Declaration
317 of Helsinki following approval of the local ethics committees. Written informed consent was
318 received from participants prior to inclusion in the study. All mouse experiments were conducted

319 according to institutional and federal guidelines and approved by the LANUV NRW VSG 84-
320 02.04.2013.A336.
321 *Statistics*
322 If not stated otherwise, unpaired two tailed Student's t-test was used to compare two groups and
323 p values ≤ 0.05 were considered significant. For multiple group comparisons, we applied 1-way
324 ANOVA followed by Tukey's post hoc correction. Statistics were performed using GraphPad Prism
325 8.
326
327 **Results:**
328 **DNA damage repair is essential for podocyte health**
329 A well-established mouse model to induce DNA damage *in vivo* is the deletion of the DNA excision
330 repair protein Ercc1, a cofactor for endonuclease Ercc4 (54–56). Our group has proposed a role
331 of DNA damage in glomerular aging by investigating glomeruli of the *Ercc1* -/delta mouse (57), a
332 model with whole body disruption of *Ercc1* on one allele and a truncated form of *Ercc1* on the
333 second allele, leading to a hypomorphic variant with minimal residual Ercc1 activity. We previously
334 showed that the expression profile of *Ercc1* -/delta glomeruli shared similarities with the profile of
335 aged glomeruli. Very recently, a shift towards small RNA transcripts as a novel hallmark of aging
336 was described (35), hence, we compared the length of RNA transcripts in prematurely aged 14-
337 week-old *Ercc1* -/delta glomeruli in comparison to WT glomeruli of the same age. RNA expression
338 showed an upregulation of the 5% and 1% shortest and downregulation of the 5% and 1% longest
339 transcripts (Fig. 1A and S1) confirming transcriptional stalling as a hallmark of the aging process
340 in *Ercc1*-deficient glomeruli (35). This glomerular phenotype coincided with the development of
341 foot process effacement, a characteristic feature of podocyte damage, detected in electron
342 microscopy (Fig. 1B), pointing towards DNA damage repair as an essential component of
343 glomerular aging and podocyte health. To specifically investigate the role of DNA damage repair
344 and aging on podocytes, we generated a constitutive podocyte-specific knockout of *Ercc1* using
345 the cre-loxP system in mice of mixed FVB/CD1 background (58) (Fig. S2A & 1C.), expecting a
346 phenotype of accelerated podocyte aging. Mice carrying the podocyte-specific *Ercc1* knockout
347 (pko) had a dramatically decreased lifespan of 15-20 weeks, while cre negative animals (ctrl) and
348 cre positive animals heterozygous for the floxed *Ercc1* allele (het) remained without overt
349 abnormalities for up to 72 weeks (Fig. 1D & S2B & C).). This decreased lifespan was accompanied
350 by significant albuminuria and severe renal failure represented by elevated serum creatinine and
351 urea levels, starting at week 11 (Fig. 1E-G). At week 13, *Ercc1* pko mice developed severe

352 generalized renal damage, including glomerulosclerosis, interstitial fibrosis, and tubular atrophy
353 with protein casts (Fig. 1H).
354 Similar results could be obtained in a tamoxifen-inducible podocyte-specific knockout (ipko) of
355 *Ercc1* (Fig. S3), indicating that this phenotype was not dependent on developmental abnormalities
356 in the absence of *Ercc1*.
357
358 **DNA damage accumulation in podocytes triggers cellular stress and podocyte loss**
359 Ultrastructural alterations in 9-week-old constitutive *Ercc1* pko glomeruli were detectable in the
360 form of focally effaced podocyte foot processes. These changes had not yet occurred in 7-week-
361 old animals (Fig. 2A). Further evidence of podocyte stress was revealed by gradual reduction of
362 nephrin abundance, an important protein of the glomerular filtration barrier, from weeks 9 to 13
363 (Fig. 2B & S4A). Podocyte number, glomerular hypertrophy, and podocyte density, investigated
364 through staining of the podocyte specific proteins synaptopodin (SNP) and Dachshund Family
365 Transcription Factor 1 (Dach1), remained within normal ranges at week 9 (Fig. 2C & S4B). In
366 contrast, glomeruli from 11-week-old *Ercc1* pko mice clearly showed severe injury and loss of
367 podocytes, indicated by the decrease and loss of both markers (Fig. 2D). This loss of podocytes
368 was further validated through the analysis of WT1-positive cells in 9- and 11-week-old *Ercc1* pko
369 mice (Fig. S4C).
370 Foci of phosphorylated histone 2A.X (γH2A.X), a *bona fide* marker for DNA double-strand breaks,
371 were significantly increased in both number and area in podocyte nuclei of *Ercc1* pko glomeruli at
372 week 9 (Fig. 2E & S4D-F) compared to control animals. Strikingly, we also observed a smaller
373 number of γH2A.X foci in almost all wildtype podocyte nuclei, indicative of constant DNA damage
374 occurrence and subsequent repair in healthy glomeruli. At later time points, single podocytes with
375 γH2A.X signals covering larger areas of the nuclei became apparent in *Ercc1* pko glomeruli (Fig.
376 2F).
377
378 **DNA damage accumulation in podocytes activates the mTORC1 pathway *in vivo***
379 Podocyte damage and loss is tightly linked to mTORC1 activation and cellular hypertrophy of the
380 remaining podocytes (10, 24, 59). Therefore, we investigated the timepoint of mTORC1 activation
381 in *Ercc1* pko mice. Interestingly, we detected a significant increase in pS6RP-positive cells in
382 *Ercc1* pko glomeruli at 9 weeks of age (Fig. 3A), a timepoint when no evidence for podocyte loss
383 was present yet (Fig. 2C & S4C). In-detail analysis revealed that more than 40% of podocytes
384 showed mTORC1 activation at week 9 (Fig. 3A).

385 To investigate whether increased mTORC1 signaling contributes to the development of podocyte
386 loss, we analysed archival kidney tissue of *Ercc1* -/delta mice treated with 14 mg/kg food of the
387 mTORC1 inhibitor rapamycin from 8 weeks of age until termination of the experiment due to high
388 moribund scoring (40). Despite the fact that the treated cohort did not have an extended lifespan,
389 moribund animals of the end-of-life cohort (aged 15-26 weeks) presented with a significant
390 reduction of sclerotic glomeruli when treated with rapamycin (Fig. 3B). Functional data through
391 blood and urine was not available for this cohort. In addition, we treated our podocyte-specific
392 *Ercc1* ko mouse model with 2 mg/kg bodyweight rapamycin via intraperitoneal injections three
393 times a week, beginning at 6 weeks of age. Again, we detected a modulation of the glomerular
394 phenotype with a significant reduction in globally sclerotic glomeruli and an increase in mildly
395 affected glomeruli upon rapamycin treatment at the end of our observation period at week 13 (Fig.
396 3C). Under these rapamycin conditions, albuminuria, serum creatinine, and serum urea levels
397 were not reduced (Fig.S5A-C). However, rapamycin therapy was accompanied by a reduction of
398 body weight to normal levels in treated animals (Fig.S5D & E), representative of a decreased rate
399 of edema (Fig.S5F).
400 The observed detection of increased mTORC1 signaling and DNA damage accumulation
401 suggests a potential interplay. It has been shown that increased mTORC1 signaling decreases
402 the cellular ability to repair DNA damage (21, 22). Thus, we investigated the occurrence of
403 increased DNA damage in a podocyte-specific *Tsc1* knockout mouse model, known to exhibit
404 mTORC1 hyperactivation, by assessing γH2A.X foci accumulation in archival kidney tissue (10,
405 39). Indeed, *Tsc1* pko mice also depicted an increased number of DNA damage foci already at 4
406 weeks of age, when the phenotype is predominantly driven by mTORC1 hyperactivation (Fig. 3D).
407 These data indicate that increased mTORC1 signaling due to DNA damage accumulation and
408 decreased DNA damage repair upon mTORC1 activation may constitute a downward spiral
409 aggravating podocyte injury (Fig. 3E).
410
411 **DNA damage activates the mTORC1 cascade through DNA damage signaling kinase DNA-**
412 **PK in podocytes**
413 To further investigate the mechanism behind mTORC1 activation occurring in podocytes upon
414 transcription stress, we induced DNA damage through mitomycin C (MMC) treatment or UV-C
415 irradiation *in vitro* in immortalized mouse podocytes (Fig. 4A). These treatments led to significant
416 increases of γH2A.X (Fig. 4B) and accumulation of the DNA damage response protein p53 in the
417 nucleus (Fig. 4C). Again, DNA damage induced an increased phosphorylation of S6 ribosomal

418 protein (pS6RP), which is a downstream target of mTORC1, in podocytes (Fig. 4D). This
419 phosphorylation was completely abrogated by mTORC1 inhibitor rapamycin and reduced by
420 serum starvation, a well-known mTORC1 modulator (60). In order to identify the link between DNA
421 damage accumulation and mTORC1 activation, we treated MMC- or UV-C-stimulated murine
422 podocytes with inhibitors of the DNA damage signaling cascade (Fig. 4E). In both conditions,
423 inhibition of DNA-dependent protein kinase (DNA-PK) by Nedisertib resulted in abrogation of
424 S6RP phosphorylation. Similar results could be achieved with the Ataxia Telangiectasia Mutated
425 serine/threonine kinase (ATM) inhibitor KU60019. No effects were detected upon treatment with
426 the ATR inhibitor VE822 or with the CHK1 inhibitor prexasertib (data not shown). These data
427 indicate a direct mechanistic link between transcription stress and mTORC1 signaling in
428 podocytes.
429
430 **DNA damage repair pathways are impaired in focal segmental glomerulosclerosis resulting**
431 **in DNA damage accumulation**
432 Since our initial goal was the analysis of podocyte aging, we investigated both murine and human
433 glomeruli of young and aged subjects. Indeed, the well-documented increase in mTORC1
434 signaling in aged murine wild-type podocytes coincided with increased detection of DNA damage
435 foci (Fig. 5A & S6A). Similar results were detected in a series of human healthy kidney tissue
436 when comparing a young (21-49 years; n=4) with an aged group (69-81 years; n=5) (Fig.5B &
437 S6B). These results confirm the occurrence of DNA damage in both healthy murine and human
438 podocytes and indicate an association between DNA damage and podocyte aging, presumably
439 contributing to age-related podocyte loss (10).
440 Furthermore, the striking podocyte phenotype upon DNA damage accumulation prompted us to
441 investigate DNA damage repair genes in different glomerular diseases. When analysing data of
442 the human renal cDNA biobank (ERCB) which contains cDNA samples of kidney biopsies, we
443 detected alterations in the expression of DNA repair genes in glomerular lysates of different
444 nephropathies compared to controls (Fig. S7; Tbl. S1), with the strongest effect in focal segmental
445 glomerulosclerosis (FSGS) and the mildest in minimal change disease (MCD). Hence, we
446 investigated the expression of DNA repair genes in podocytes of human FSGS biopsies, minimal
447 change disease (MCD) and healthy controls of a single nucleus RNA sequencing data set (50)
448 (Fig. 5C). Indeed, we detected an upregulation in *Ercc1-8* genes, all involved in damage
449 recognition, DNA unwinding, and damage excision (Fig. 5D, E & S8) in FSGS podocytes. This
450 upregulation indicates that podocytes increase their machinery to repair DNA damage in the

451 presence of FSGS. Vice versa, the expression of several subunits of RNA polymerase 2 and the
452 shared subunit of RNA polymerases 1-3, POL2RK, were virtually lost in human podocytes of both
453 MCD and FSGS samples (Fig 5D, F & S8). These expression data indicate a predominance of
454 damage recognition and strand excision in FSGS biopsies with the potential of downregulation /
455 stalling of RNA synthesis. Targets of the mTORC1 pathway served as an internal control, depicting
456 increased expression with little changes in the percentage of podocytes expressing these genes
457 (Fig. 5D).
458 To further elucidate this observation of perturbed DNA damage recognition, we investigated the
459 accumulation of DNA damage in podocyte nuclei of human biopsies of FSGS compared to MCD
460 patients using γH2A.X immunofluorescence staining. Indeed, we detected a marked increase in
461 podocyte-specific nuclear γH2A.X foci in FSGS glomeruli (Fig. 5G) corresponding to increased
462 DNA double-strand breaks and thus suggestive of an involvement of DNA damage accumulation
463 in human glomerular disease with marked podocyte damage and loss.
464 In line with this, using an expression quantitative trait locus (eQTL) analysis, we identified single
465 nucleotide polymorphisms (SNPs) associated with alterations in the expression of DNA repair
466 genes (Table S2 – S4) in sclerotic glomerular diseases that could be targets of interest for future
467 investigations and also for therapeutic modulation.
468
469 **Discussion**:
470 To which extent glomerular epithelial cells are subject to transcription stress is currently unclear.
471 Elucidating this subject is of particular interest for podocytes, terminally differentiated cells with a
472 limited ability to self-renew (7). These cells have to maintain a functional genome for the
473 organism's entire life-span, specifically important in the later stages of life. For the first time, our
474 study reveals the occurrence of DNA damage foci in individual podocytes under healthy
475 conditions, indicating a need for constant DNA maintenance and repair and an increase of DNA
476 damage in aged podocytes. Furthermore, we show that this accumulation of DNA damage results
477 in the newly established principle of transcriptional stalling and a shift to the expression of shorter
478 transcripts in glomeruli (35). Recent studies have indicated that the aged podocyte phenotype is
479 in part characterized by senescence. Transcriptomic analysis detected differential expression of
480 senescence-associated genes in aged podocytes (61) coinciding with increased gene silencing.
481 This senescence phenotype was shown to be driven by GSK3 beta overexpression and inhibition
482 via lithium could improve podocyte aging in mice and decrease podocyturia in humans (62). This
483 fits well to the interplay of DNA damage and GSK3 beta activation, as GSK3 beta was shown to

484 be involved DNA damage repair in cancer and that its nuclear translocation was, in part,
485 dependent on p53 activation and nuclear translocation (63–65). A potential causal chain for the
486 senescent phenotype could, therefore, be the activation of GSK3 beta signaling due to DNA
487 damage accumulation in aged podocytes.
488 The response to transcriptomic stress in podocytes was different from the pattern reported in other
489 cell types, as podocytes activated mTORC1 signaling upon DNA damage. The interplay of DNA
490 damage, its repair, and the mTOR pathway has been a subject of numerous studies, specifically
491 in the field of cancer biology. These studies indicated that mTORC1 signaling is inhibited upon
492 DNA damage in a TSC, Sestrin or AKT-dependent manner (18)(19)(20). Strikingly, we observed
493 that podocytes both *in vitro* and *in vivo* reacted to endogenous accumulation or exogenous
494 infliction of DNA damage with activation of the mTORC1 pathway. Herein lies a fundamental
495 difference to past reports and a potential disease mechanism as numerous studies have depicted
496 the importance of a tight regulation of mTORC1 for podocyte health and the deleterious effects of
497 both overactivation and repression in disease (10, 24, 26, 44, 59, 66). Since mTORC1 activation
498 occurs in *Ercc1* pko podocytes at 9 weeks, a time point of no overt podocyte loss, mild
499 ultrastructural differences, and significant accumulation of DNA damage foci, our data indicate a
500 link between transcription stress and mTORC1 activation in podocytes. This activation occurs via
501 activation of DNA-PK, a nuclear serine/threonine protein kinase.
502 A growing body of evidence suggests that mTORC1 activity reduces the capacity of successful
503 DNA repair (21, 22), e.g. through ribosomal S6 kinase (S6K)-dependent phosphorylation of E3
504 ubiquitin-protein ligase RNF168 (23). However, upon podocyte depletion, remaining podocytes on
505 the glomerular tuft counteract the loss of neighbouring cells through mTORC1-mediated
506 hypertrophy (10) which impairs proper DNA repair. This fact is underlined by podocyte-specific
507 *Tsc1* knockout animals displaying mTORC1 hyperactivation. These animals accumulate a
508 significant amount of DNA damage foci already at 4 weeks of age. We, therefore, hypothesize that
509 the interplay of DNA damage and mTORC1 signaling can lead to a downward spiral: accumulation
510 of DNA damage in podocytes triggers mTORC1 activation which further aggravates insufficient
511 DNA maintenance leading to excessive podocyte loss. This cascade could potentially be
512 modulated through well-timed mTORC1 inhibition as suggested by the reduction of
513 glomerulosclerosis in rapamycin-treated *Ercc1* -/delta and *Ercc1* pko animals or by upregulation
514 of DNA repair mechanisms to alleviate accumulated transcription stress.
515 Only recently the importance of DNA repair has sparked larger interest in the field of podocyte
516 biology. The description of glomerular abnormalities in human syndromes caused by mutations in

517 DNA repair genes is scarce due to their frequently lethal phenotypes (67, 68). First evidence of
518 ERCC1 being an essential protein in kidney health was recently provided through the identification
519 of *ERCC1* variants causing proximal tubular dysfunction as well as glomerular disease underlined
520 by albuminuria in the reported patients (69). Data from whole body *Ercc1* null mice with correction
521 of the liver phenotype also indicate a role for glomerular health with *Ercc1*-deficient animals rapidly
522 dying of renal failure (70). Beyond that, there is evidence for podocyte involvement in human
523 syndromes caused by mutations of DNA repair genes with patients exhibiting proteinuria and
524 nephrotic syndrome (55, 71, 72). Consistently, gene deletion of DNA repair endonuclease co-
525 factor *Ercc1* in podocytes caused proteinuria and FSGS in our mouse model.
526 The same holds true for factors involved in other forms of DNA maintenance such as the KEOPS
527 complex (14, 73), KAT5 (74), and SMPDL3b in podocytes, playing a role in DNA damage
528 recognition (75). Recently, these processes were shown to extend towards epigentic effects, as
529 HDAC deletion in podocytes resulted in DNA damage accumulation, senescence, cell cycle
530 reentry, and FSGS (76). Itoh and co-workers linked proteinuric kidney disease present in patients
531 with hypertension and diabetes to DNA double-strand breaks and methylation in the promotor
532 region of the slit diaphragm protein nephrin, and established an association to DNA double-strand
533 breaks in glomeruli of patients suffering from IgA nephropathy (15, 16). Our analysis adds
534 considerably to this body of evidence, as we identified multiple factors of DNA maintenance to be
535 transcriptionally altered in glomeruli and single podocytes of different renal diseases involving
536 pronounced podocyte damage and loss, such as MCD and FSGS. Interestingly, we found
537 increased expression of DNA repair proteins in focal segmental glomerulosclerosis (FSGS),
538 suggesting that increased transcription stress may contribute to the loss of podocytes in renal
539 disease. This is in line with altered expression of endonuclease ERCC4 in IgA nephropathy (15).
540 Our study complements these data suggesting that loss of especially transcription-coupled
541 nucleotide excision repair capacity, which removes lesions from the template DNA strands of
542 actively transcribed genes, may contribute to the progression of some types of glomerular disease
543 and aging. The importance of DNA damage repair in podocyte homeostasis is consistent with the
544 role in other postmitotic cell types and particularly apparent in neurodegenerative pathologies
545 typical for DNA repair deficiency syndromes (5). Repairing transcription-blocking lesions might
546 thus play a pivotal role in podocytes as post-mitotic cells that need to maintain the integrity of
547 transcribed genes during the entire lifespan of the organism. Even hepatocytes of *Ercc1* -/delta
548 mice, usually characterized by high self-renewing potential, showed a considerable block of
549 transcription, indicative of transcription-coupled mechanisms being stalled (50, 77). Potential sites

550 in the genome that may be used to alter glomerular damage repair were already identified in our
551 expression quantitative trait locus (eQTL) analysis in FSGS patients. This is of particular interest
552 since there seems to be a broad interplay between gene products exerting functions beyond their
553 canonical pathways in genome maintenance (78). Likewise, decreased expression of DNA repair
554 genes in a subset of patients or the accumulation of DNA damage through the aging process may
555 lead to increased mTORC1 activation in podocytes, thereby rendering a subgroup of patients
556 vulnerable to the development of glomerular disease and scarring.
557 In conclusion, we identified efficient DNA damage repair as an essential stress response
558 mechanism for podocyte homeostasis and established a link between DNA damage accumulation
559 and mTORC1 signaling. Furthermore, the presented study identifies transcription stress as a
560 hallmark of podocyte aging, loss, and glomerular disease, suitable for precision medicine
561 approaches.
562
563 **Disclosures:**
564 The authors declare no conflict of interest.
565
566 **Author contributions:**
567 FB, AMM, LB, RAH, VGP, DM, MNW, GC, MR, DF, GGS, SK, MTL, WB, VN, PM performed
568 experiments; FB, LB, AMM, GC, RAH, VGP, MNW, DF, MTL, WB, MGS, VN analysed data; FB,
569 AMM, VGP, GG, MD, PTB, CDC, MK, MGS, MK, TBH, BSche, TB, BSchu, CEK conceived
570 experiments, FB, VGP, BSchu, CEK wrote the manuscript, all authors revised the manuscript, all
571 authors agreed on the publication in the presented state.
572
573 Funding:
574 Fabian Braun received funding from the Else-Kröner-Fresenius-Stiftung: Else-Kröner-Memorial
575 Stipendium / 2021_EKMS.26
576 Amrei M. Mandel was partially funded by the Else Kröner-Fresenius-Stiftung and the Eva Luise
577 und Horst Köhler Stiftung – Project No: 2019_KollegSE.04.
578 Linda Blomberg was supported by the Faculty of Medicine, University of Cologne: Koeln Fortune
579 Program KF 12/2020.
580 Victor Puelles received support from the Deutsche Forschungsgemeinschaft: Clinical Research
581 Unit / CRC1192, and the Bundesministerium für Bildung und Forschung eMed Consortia /
582 Fibromap) and the Novo Nordisk Foundation (NNF21OC0066381).

583 Georgia Chatzinikolaou is supported by ELIDEK grant agreement No 1059, funded from the
584 Hellenic Foundation for Research and Innovation (HFRI) and the General Secretariat for Research
585 and Technology (GSRT).
586 Gisela G. Slaats was supported by an EMBO long-term fellowship ALTF 475-2016 and the Fritz
587 Thyssen Foundation project 10.20.1.012MN.
588 Martijn Dollé received support the National Institute of Health (NIH)/National Institute of Aging
589 (NIA) (AG17242)
590 Paul T. Brinkkoetter received support from the Deutsche Forschungsgemeinschaft: Clinical
591 research unit: KFO 329, BR 2955/8-1, and the Bundesministerium für Bildung und Forschung
592 STOP-FSGS 01GM1901E
593 Matthew G. Samspon is supported by NIH grants RO1 DK108805, DK119380, and RC2
594 DK122397
595 George A. Garinis was supported by ELIDEK grant 631, funded from the Hellenic Foundation for
596 Research and Innovation (HFRI).
597 The George M. O'Brien Michigan Kidney Translational Core Center was funded by NIH/NIDDK
598 grant 2P30-DK-081943.
599 Bernhard Schermer received support by the Deutsche Forschungsgemeinschaft: Clinical research
600 unit KFO 329 SCHE 1562/7-1.
601 Thomas Benzing received support from the Deutsche Forschungsgemeinschaft: Clinical research
602 unit: KFO 329, BE 2212/23-1 & 2212/24-1, and the Bundesministerium für Bildung und Forschung
603 STOP-FSGS 01GM1901E
604 Christine Kurschat received support by the Deutsche Forschungsgemeinschaft: Clinical research
605 unit KFO 329 KU 1539/5-1.
606
607 **References:**
608

609 1. Lindahl T, Nyberg B. Rate of depurination of native deoxyribonucleic acid. *Biochemistry-us*
610 1972;11(19):3610–3618.

611 2. Loeb LA, Harris CC. Advances in chemical carcinogenesis: a historical review and
612 prospective.. *Cancer Res* 2008;68(17):6863–72.

613 3. Chatterjee N, Walker GC. Mechanisms of DNA damage, repair, and mutagenesis: DNA
614 Damage and Repair. *Environ Mol Mutagen* 2017;58(5):235–263.

615 4. Ghosal G, Chen J. DNA damage tolerance: a double-edged sword guarding the genome..
616 *Transl Cancer Res* 2013;2(3):107–129.

617 5. Wolters S, Schumacher B. Genome maintenance and transcription integrity in aging and
618 disease. *Frontiers Genetics* 2013;4:19.

619 6. Madabhushi R, Pan L, Tsai L-H. DNA damage and its links to neurodegeneration.. *Neuron*
620 2014;83(2):266–82.

621 7. Wanner N, et al. Unraveling the role of podocyte turnover in glomerular aging and injury..
622 *Journal of the American Society of Nephrology : JASN* 2014;25(4):707–716.

623 8. Butt L, et al. A molecular mechanism explaining albuminuria in kidney disease. *Nat*
624 *Metabolism* 2020;2(5):461–474.

625 9. Chen TK, Knicely DH, Grams ME. Chronic Kidney Disease Diagnosis and Management.
626 *Jama* 2019;322(13):1294–1304.

627 10. Puelles VG, et al. mTOR-mediated podocyte hypertrophy regulates glomerular integrity in
628 mice and humans. *Jci Insight* 2019;4(18):e99271.

629 11. Rosenberg AZ, Kopp JB. Focal Segmental Glomerulosclerosis.. *Clinical journal of the*
630 *American Society of Nephrology : CJASN* 2017;12(3):502–517.

631 12. Marshall CB, et al. Puromycin aminonucleoside induces oxidant-dependent DNA damage in
632 podocytes in vitro and in vivo. *Kidney Int* 2006;70(11):1962–1973.

633 13. Hakroush S, et al. Extensive Podocyte Loss Triggers a Rapid Parietal Epithelial Cell
634 Response. *Journal of the American Society of Nephrology : JASN* 2014;25(5):927–938.

635 14. Braun DA, et al. Mutations in KEOPS-complex genes cause nephrotic syndrome with
636 primary microcephaly.. *Nature genetics* 2017;49(10):1529–1538.

637 15. Hayashi K, et al. Association of glomerular DNA damage and DNA methylation with one-year
638 eGFR decline in IgA nephropathy. *Sci Rep-uk* 2020;10(1):237.

639 16. Hishikawa A, et al. DNA damage and expression of DNA methylation modulators in urine-
640 derived cells of patients with hypertension and diabetes.. *Sci Rep-uk* 2020;10(1):3377.

641 17. Schermer B, et al. Transcriptional profiling reveals progeroid Ercc1-/Δ mice as a model
642 system for glomerular aging. *Bmc Genomics* 2013;14(1):559.

643 18. Reiling JH, Hafen E. The hypoxia-induced paralogs Scylla and Charybdis inhibit growth by
644 down-regulating S6K activity upstream of TSC in Drosophila. *Gene Dev* 2004;18(23):2879–
645 2892.

646 19. Budanov AV, Karin M. p53 Target Genes Sestrin1 and Sestrin2 Connect Genotoxic Stress
647 and mTOR Signaling. *Cell* 2008;134(3):451–460.

648 20. Wu D-D, et al. PEST-containing nuclear protein mediates the proliferation, migration, and
649 invasion of human neuroblastoma cells through MAPK and PI3K/AKT/mTOR signaling
650 pathways.. *Bmc Cancer* 2018;18(1):499.

651 21. Chebel A, et al. Rapamycin safeguards lymphocytes from DNA damage accumulation in
652 vivo.. *European journal of cell biology* 2016;95(9):331–341.

653 22. Dominick G, et al. mTOR regulates the expression of DNA damage response enzymes in
654 long-lived Snell dwarf, GHRKO, and PAPPA-KO mice.. *Aging Cell* 2016;16(1):52–60.

655 23. Xie X, et al. The mTOR–S6K pathway links growth signalling to DNA damage response by
656 targeting RNF168. *Nat Cell Biol* 2018;20(3):320–331.

657 24. Zschiedrich S, et al. Targeting mTOR Signaling Can Prevent the Progression of FSGS..
658 *Journal of the American Society of Nephrology : JASN* 2017;28(7):2144–2157.

659 25. Nishizono R, et al. FSGS as an Adaptive Response to Growth-Induced Podocyte Stress..
660 *Journal of the American Society of Nephrology : JASN* 2017;28(10):2931–2945.

661 26. Inoki K, et al. mTORC1 activation in podocytes is a critical step in the development of
662 diabetic nephropathy in mice.. *The Journal of clinical investigation* 2011;121(6):2181–2196.

663 27. Kurayama R, et al. Role of amino acid transporter LAT2 in the activation of mTORC1
664 pathway and the pathogenesis of crescentic glomerulonephritis. *Lab Invest* 2011;91(7):992–
665 1006.

666 28. Dittrich E, et al. Rapamycin-associated post-transplantation glomerulonephritis and its
667 remission after reintroduction of calcineurin-inhibitor therapy. *Transplant Int* 2004;17(4):215–220.

668 29. Butani L. Investigation of Pediatric Renal Transplant Recipients with Heavy Proteinuria after
669 Sirolimus Rescue. *Transplantation* 2004;78(9):1362–1366.

670 30. Izzedine H, Brocheriou I, Frances C. Post-Transplantation Proteinuria and Sirolimus. *New*
671 *Engl J Med* 2005;353(19):2088–2089.

672 31. Sennesael JJ, et al. Conversion from Cyclosporine to Sirolimus in Stable Renal Transplant
673 Recipients. *Transplantation* 2005;80(11):1578–1585.

674 32. Letavernier E, et al. High Sirolimus Levels May Induce Focal Segmental Glomerulosclerosis
675 De Novo. *Clin J Am Soc Nephro* 2007;2(2):326–333.

676 33. Cho ME, Hurley JK, Kopp JB. Sirolimus Therapy of Focal Segmental Glomerulosclerosis Is
677 Associated With Nephrotoxicity. *Am J Kidney Dis* 2007;49(2):310–317.

678 34. Hochegger K, et al. Differential Effects of Rapamycin in Anti-GBM Glomerulonephritis. *J Am*
679 *Soc Nephrol* 2008;19(8):1520–1529.

680 35. Gyenis A, et al. Genome-wide RNA polymerase stalling shapes the transcriptome during
681 aging. *Nat Genet* 2023;55(2):268–279.

682 36. Irizarry RA, et al. Exploration, normalization, and summaries of high density oligonucleotide
683 array probe level data.. *Biostatistics (Oxford, England)* 2003;4(2):249–264.

684 37. Ritchie ME, et al. limma powers differential expression analyses for RNA-sequencing and
685 microarray studies. *Nucleic Acids Res* 2015;43(7):e47–e47.

686 38. Yu G, et al. clusterProfiler: an R Package for Comparing Biological Themes Among Gene
687 Clusters. *Omics J Integr Biology* 2012;16(5):284–287.

688 39. Bork T, et al. Podocytes maintain high basal levels of autophagy independent of mtor
689 signaling. *Autophagy* 2019;16(11):1–17.

690 40. Birkisdóttir MB, et al. Unlike dietary restriction, rapamycin fails to extend lifespan and reduce
691 transcription stress in progeroid DNA repair-deficient mice. *Aging Cell* 2021;20(2):e13302.

692 41. Rinschen MM, et al. A Multi-layered Quantitative In Vivo Expression Atlas of the Podocyte
693 Unravels Kidney Disease Candidate Genes.. *Cell reports* 2018;23(8):2495–2508.

694 42. Puelles VG, et al. Podocyte Number in Children and Adults: Associations with Glomerular
695 Size and Numbers of Other Glomerular Resident Cells. *J Am Soc Nephrol* 2015;26(9):2277–
696 2288.

697 43. Endlich N, et al. The transcription factor Dach1 is essential for podocyte function. *J Cell Mol*
698 *Med* 2018;22(5):2656–2669.

699 44. Liebau MC, et al. Dysregulated Autophagy Contributes to Podocyte Damage in Fabry's
700 Disease. *Plos One* 2013;8(5):e63506.

701 45. Shankland SJ, et al. Podocytes in culture: past, present, and future. *Kidney international*
702 2007;72(1):26–36.

703 46. Liberzon A, et al. The Molecular Signatures Database Hallmark Gene Set Collection. *Cell*
704 *Syst* 2015;1(6):417–425.

705 47. Cohen CD, et al. Quantitative gene expression analysis in renal biopsies: A novel protocol
706 for a high-throughput multicenter application. *Kidney Int* 2002;61(1):133–140.

707 48. Cohen CD, et al. Comparative promoter analysis allows de novo identification of specialized
708 cell junction-associated proteins. *Proc National Acad Sci* 2006;103(15):5682–5687.

709 49. Tusher VG, Tibshirani R, Chu G. Significance analysis of microarrays applied to the ionizing
710 radiation response.. *Proceedings of the National Academy of Sciences of the United States of*
711 *America* 2001;98(9):5116–5121.

712 50. Mariani LH, et al. Precision nephrology identified tumor necrosis factor activation variability in
713 minimal change disease and focal segmental glomerulosclerosis.. *Kidney Int* [published online
714 ahead of print: 2022]; doi:10.1016/j.kint.2022.10.023

715 51. Shabalin AA. Matrix eQTL: ultra fast eQTL analysis via large matrix operations.
716 *Bioinformatics* 2012;28(10):1353–1358.

717 52. Stegle O, et al. A Bayesian Framework to Account for Complex Non-Genetic Factors in
718 Gene Expression Levels Greatly Increases Power in eQTL Studies. *Plos Comput Biol*
719 2010;6(5):e1000770.

720 53. Wen X, et al. Efficient Integrative Multi-SNP Association Analysis via Deterministic
721 Approximation of Posteriors. *Am J Hum Genetics* 2016;98(6):1114–1129.

722 54. Niedernhofer LJ, et al. A new progeroid syndrome reveals that genotoxic stress suppresses
723 the somatotroph axis.. *Nature* 2006;444(7122):1038–1043.

724 55. Doig J, et al. Mice with skin-specific DNA repair gene (Ercc1) inactivation are hypersensitive
725 to ultraviolet irradiation-induced skin cancer and show more rapid actinic progression..
726 *Oncogene* 2006;25(47):6229–6238.

727 56. Karakasilioti I, et al. DNA Damage Triggers a Chronic Autoinflammatory Response, Leading
728 to Fat Depletion in NER Progeria. *Cell Metabolism* 2013;18(3):403–415.

729 57. Weeda G, et al. Disruption of mouse ERCC1 results in a novel repair syndrome with growth
730 failure, nuclear abnormalities and senescence.. *Current biology : CB* 1997;7(6):427–439.

731 58. Moeller MJ, et al. Podocyte-specific expression of cre recombinase in transgenic mice.
732 *Genesis (New York, N.Y. : 2000)* 2003;35(1):39–42.

733 59. Gödel M, et al. Role of mTOR in podocyte function and diabetic nephropathy in humans and
734 mice.. *The Journal of clinical investigation* 2011;121(6):2197–2209.

735 60. Settembre C, et al. Signals from the lysosome: a control centre for cellular clearance and
736 energy metabolism. *Nature Reviews Molecular Cell Biology* 2013;14(5):283–296.

737 61. Wang Y, et al. Global transcriptomic changes occur in aged mouse podocytes.. *Kidney Int*
738 [published online ahead of print: 2020]; doi:10.1016/j.kint.2020.05.052

739 62. Fang Y, et al. Age-related GSK3β overexpression drives podocyte senescence and
740 glomerular aging. *J Clin Invest* 2022;132(4):e141848.

741 63. Zhang N, et al. Glycogen synthase kinase 3β inhibition synergizes with PARP inhibitors
742 through the induction of homologous recombination deficiency in colorectal cancer. *Cell Death*
743 *Dis* 2021;12(2):183.

744 64. Yang Y, et al. Nuclear GSK3β induces DNA double-strand break repair by phosphorylating
745 53BP1 in glioblastoma. *Int J Oncol* 2018;52(3):709–720.

746 65. Ngok-Ngam P, et al. Pharmacological inhibition of GSK3 attenuates DNA damage-induced
747 apoptosis via reduction of p53 mitochondrial translocation and Bax oligomerization in
748 neuroblastoma SH-SY5Y CELLS. *Cell Mol Biology Lett* 2013;18(1):58–74.

749 66. Ising C, et al. Inhibition of insulin/IGF-1 receptor signaling protects from mitochondria-
750 mediated kidney failure.. *EMBO Molecular Medicine* 2015;7(3):275–287.

751 67. Hirooka M, Hirota M, Kamada M. Renal lesions in Cockayne syndrome. *Pediatr Nephrol*
752 1988;2(2):239–243.

753 68. Chehida AB, et al. Renal Involvement in 2 Siblings With Cockayne Syndrome.. *Iran J Kidney*
754 *Dis* 2017;11(3):253–255.

755 69. Apelt K, et al. ERCC1 mutations impede DNA damage repair and cause liver and kidney
756 dysfunction in patients. *J Exp Med* 2020;218(3). doi:10.1084/jem.20200622

757 70. Selfridge J, et al. Correction of liver dysfunction in DNA repair-deficient mice with an ERCC1
758 transgene. *Nucleic Acids Res* 2001;29(22):4541–4550.

759 71. Faridounnia M, et al. The Cerebro-Oculo-Facio-Skeletal (COFS) Syndrome point mutation
760 F231L in the ERCC1 DNA repair protein causes dissociation of the ERCC1-XPF complex..
761 *Journal of Biological Chemistry* [published online ahead of print: June 17, 2015];
762 doi:10.1074/jbc.m114.635169

763 72. Kondo D, et al. Elevated Urinary Levels of 8-Hydroxy-2'-deoxyguanosine in a Japanese
764 Child of Xeroderma Pigmentosum/Cockayne Syndrome Complex with Infantile Onset of
765 Nephrotic Syndrome.. *Tohoku J Exp Medicine* 2016;239(3):231–5.

766 73. Hecker A, et al. The universal Kae1 protein and the associated Bud32 kinase (PRPK), a
767 mysterious protein couple probably essential for genome maintenance in Archaea and Eukarya.
768 *Biochem Soc T* 2009;37(1):29–35.

769 74. Hishikawa A, et al. Decreased KAT5 Expression Impairs DNA Repair and Induces Altered
770 DNA Methylation in Kidney Podocytes.. *Cell reports* 2019;26(5):1318-1332.e4.

771 75. Francis M, et al. SMPDL3b modulates radiation-induced DNA damage response in renal
772 podocytes. *Faseb J* 2022;36(10):e22545.

773 76. Rangel PXM, et al. Cell Cycle and Senescence Regulation by Podocyte Histone
774 Deacetylase 1 and 2. *J Am Soc Nephrol* 2023;34(3):433–450.

775 77. Milanese C, et al. DNA damage and transcription stress cause ATP-mediated redesign of
776 metabolism and potentiation of anti-oxidant buffering. *Nat Commun* 2019;10(1):4887.

777 78. Mulderrig L, Garaycoechea JI. XPF-ERCC1 protects liver, kidney and blood homeostasis
778 outside the canonical excision repair pathways.. *Plos Genet* 2020;16(4):e1008555.

779

780 **Acknowledgments:**

781 The excellent technical expertise of Martyna Brütting, Melanie Schaper, Anja Obser, Ilka
782 Edenhofer and Bhawani Nagarajah is gratefully acknowledged. The DNA damage response
783 inhibitors used in this study were a kind gift of Ron Jachimowicz. All schematics in figures were

784 created with BioRender.com. The ERCB-KFB was supported by the Else Kröner-Fresenius
785 Foundation. We also thank all participating centres of the European Renal cDNA Bank - Kröner-
786 Fresenius biopsy bank (ERCB-KFB) and their patients for their cooperation. Active members at
787 the time of the study see (N. Shved et al., Scientific reports 7, 8576 (2017)). The Nephrotic
788 Syndrome Study Network (NEPTUNE) is part of the Rare Diseases Clinical Research
789 Network (RDCRN), which is funded by the National Institutes of Health (NIH) and led by
790 the National Center for Advancing Translational Sciences (NCATS) through its Division of Rare
791 Diseases Research Innovation (DRDRI). NEPTUNE is funded under grant number U54DK083912
792 as a collaboration between NCATS and the National Institute of Diabetes and Digestive and
793 Kidney Diseases (NIDDK). Additional funding and/or programmatic support is provided by the
794 University of Michigan, NephCure Kidney International and the Halpin Foundation. RDCRN
795 consortia are supported by the RDCRN Data Management and Coordinating Center (DMCC),
796 funded by NCATS and the National Institute of Neurological Disorders and Stroke (NINDS) under
797 U2CTR002818.
798 Funding support for the DMCC is provided by NCATS and the National Institute of Neurological
799 Disorders and Stroke (NINDS).
800 Members of the Nephrotic Syndrome Study Network (NEPTUNE)
801 **Members of the Nephrotic Syndrome Study Network (NEPTUNE)**
802 NEPTUNE Enrolling Centers
803 *Cleveland Clinic, Cleveland, OH*: K Dell[*], J Sedor[**], M Schachere[#], J Negrey[#]
804 *Children's Hospital, Los Angeles, CA*: K Lemley[*], S Tang[#]
805 *Children's Mercy Hospital, Kansas City, MO*: T Srivastava[*], S Morrison[#]
806 *Cohen Children's Hospital, New Hyde Park, NY:* C Sethna[*], M Pfaiff [#]
807 *Columbia University, New York, NY:* P Canetta[*], A Pradhan[#]
808 *Emory University, Atlanta, GA:* L Greenbaum[*], C Wang**, E Yun[#]
809 *Harbor-University of California Los Angeles Medical Center:* S Adler[*], J LaPage[#]
810 *John H. Stroger Jr. Hospital of Cook County, Chicago, IL:* A Athavale[*], M Itteera
811 *Johns Hopkins Medicine, Baltimore, MD:* M Atkinson[*], T Dell[#]
812 *Mayo Clinic, Rochester, MN:* F Fervenza[*], M Hogan**, J Lieske[*], V Chernitskiy[#]
813 *Montefiore Medical Center, Bronx, NY:* F Kaskel[*], M Ross[*], P Flynn[#]
814 *NIDDK Intramural, Bethesda MD:* J Kopp[*], J Blake[#]
815 *New York University Medical Center, New York, NY:* L Malaga-Dieguez[*], O Zhdanova**, F
816 Modersitzki[#], L Pehrson[#]

817 *Stanford University, Stanford, CA:* R Lafayette*, B Yeung#
818 *Temple University, Philadelphia, PA:* I Lee*, S Quinn-Boyle#
819 *University Health Network Toronto:* H Reich *, M Hladunewich**, P Ling#, M Romano#
820 *University of Miami, Miami, FL:* A Fornoni*, C Bidot#
821 *University of Michigan, Ann Arbor, MI:* M Kretzler*, D Gipson*, A Williams#, C Klida#
822 *University of North Carolina, Chapel Hill, NC:* V Derebail*, K Gibson*, A Froment#, S Kelley#
823 *University of Pennsylvania, Philadelphia, PA:* L Holzman*, K Meyers**, K Kallem#, A Swenson#
824 *University of Texas Southwestern, Dallas, TX:* K Sambandam*, K Aleman#, M Rogers#
825 *University of Washington, Seattle, WA:* A Jefferson*, S Hingorani**, K Tuttle**§, M Bray #, E Pao#,
826 A Cooper#§
827 *Wake Forest University Baptist Health, Winston-Salem, NC:* JJ Lin*, Stefanie Baker#
828
829 *Data Analysis and Coordinating Center*: M Kretzler*, L Barisoni**, C Gadegbeku**, B Gillespie**,
830 D Gipson**, L Holzman**, L Mariani**, M Sampson**, J Sedor**, J Zee**, G Alter, H Desmond, S
831 Eddy, D Fermin, M Larkina, S Li, S Li, CC Lienczewski, T Mainieri, R Scherr, A Smith, A
832 Szymanski, A Williams.
833
834 *Digital Pathology Committee*: Carmen Avila-Casado (University Health Network, Toronto), Serena
835 Bagnasco (Johns Hopkins University), Joseph Gaut (Washington University in St Louis), Stephen
836 Hewitt (National Cancer Institute), Jeff Hodgin (University of Michigan), Kevin Lemley (Children's
837 Hospital of Los Angeles), Laura Mariani (University of Michigan), Matthew Palmer (University of
838 Pennsylvania), Avi Rosenberg (Johns Hopkins University), Virginie Royal (University of Montreal),
839 David Thomas (University of Miami), Jarcy Zee (University of Pennsylvania) Co-Chairs: Laura
840 Barisoni (Duke University) and Cynthia Nast (Cedar Sinai).
841
842 *Principal Investigator; **Co-investigator; #Study Coordinator
843 §Providence Medical Research Center, Spokane, WA
844
845 **Figures and Figure Legends:**
846
847 **Figure 1: The podocyte-specific constitutive ko of *Ercc1* causes glomerulosclerosis.**
848 A: GSEA of gene classes according to transcript length. Shown are the analyses for the shortest 5 % (top
849 left), shortest 1 % (top right), longest 5% (bottom left), and longest 1% (bottom right) of genes. The bottom
850 color-coded panel shows the log2 fold changes of the microarray data in a ranked order. The top panels
851 show the running enrichment score as an orange line. The smallest 1% (normalized enrichment score (NES)

852 of 2.01) and 5% (NES of 1.37) of genes are significantly enriched in the upregulated genes, while the longest
853 1% (NES of -1.69) and 5% (NES of -1.42) of genes are significantly enriched in the downregulated genes
854 in the comparison *Ercc1* -/delta 14 weeks vs. WT 14 weeks.
855 B: Representative electron microscopy image of 14-week-old wild-type (WT) and *Ercc1* -/delta glomerular
856 filtration barrier, scalebar indicating 2 μm, B: blood side – intracapillary space, U: urinary side – bowman's
857 space, asterisk indicating podocyte foot process (n=4).
858 C: qPCR analysis for *Ercc1* in FACS-sorted podocytes of *Ercc1* ctrl, wt/pko (het) or pko mice. Delta-Delta-
859 CT values expressed as scatterplots depicting mean plus 95% confidence interval.
860 D: Kaplan-Meyer curve depicting survival of *Ercc1* ctrl, wt/pko (het) and pko mice (Mantel-Cox test).
861 E: urinary albumin/creatinine analysis; F: serum creatinine analysis; G: serum urea analysis of *Ercc1* ctrl
862 and pko mice.
863 H: Representative Periodic Acid Schiff (PAS) staining of 13-week-old *Ercc1* ctrl and pko mice and
864 quantification of sclerotic glomeruli, scalebars: 100 μm, n = 5, 50 glomeruli per sample.
865 Scatterplots indicate mean plus 95% confidence interval, *p ≤ 0,05, **p ≤ 0,01, ***p ≤ 0,001, ****p ≤ 0,0001.
866
867 **Figure 2: The podocyte-specific constitutive ko of *Ercc1* leads to foot process effacement and**
868 **podocyte loss accompanied by accumulation of DNA damage.**
869 A: Representative electron microscopy image of 7- and 9-week-old *Ercc1* ctrl and pko slit diaphragms,
870 scalebar indicating 2 μm, B: blood side – intracapillary space, U: urinary side – Bowman's space, asterisk
871 indicating podocyte foot process (n=3).
872 B: Representative immunofluorescence staining of slit diaphragm protein nephrin (yellow) with nuclear
873 marker DAPI (grey) of *Ercc1* ctrl at 13 weeks of age and pko kidneys at 7, 9, 11, and 13 weeks of age,
874 scalebar indicating 2 μm (n=5).
875 C: Representative immunofluorescence staining of podocyte proteins synaptopodin (SNP, gray),
876 Dachshund homolog 1 (Dach1, green) (43) and far-red fluorescent DNA dye Draq5 (red) as a nuclear marker
877 in sections of 9-week-old *Ercc1* ctrl and pko kidneys, with quantification of podocyte number and density of
878 *Ercc1* ctrl and pko kidneys, scalebar indicating 10 μm (n=5).
879 D: Corresponding staining of podocyte proteins synaptopodin (gray), Dachshund homolog 1 (Dach1, green)
880 (43) and far-red fluorescent DNA dye Draq5 (red) as a nuclear marker in paraffin-embedded sections of 11-
881 week-old *Ercc1* ctrl and pko kidneys, scalebar indicating 10 μm (n=5).
882 E: Representative immunofluorescence staining of synaptopodin (SNP, gray), DNA damage marker γH2A.X
883 (green) and nuclear marker Draq5 (red) in sections of 9-week-old *Ercc1* ctrl and pko kidneys, with
884 quantification of γH2A.X foci per podocyte nucleus and nuclear area of *Ercc1* ctrl and pko kidneys, scalebar
885 indicating 2 μm, yellow dotted line indicating nuclear border, n=5, 10 glomeruli per sample, 5 podocytes per
886 glomerulus.
887 F: Representative immunofluorescence staining of synaptopodin (SNP, gray), DNA damage marker γH2A.X
888 (green) and nuclear marker Draq5 (red) in sections of 11-week-old *Ercc1* ctrl and pko kidneys, with
889 quantification of γH2A.X foci per podocyte nucleus and nuclear area of *Ercc1* ctrl and pko kidneys, scalebar
890 indicating 2 μm, n=5, 10 glomeruli per sample, 5 podocytes per glomerulus.
891 All violin plots indicate median (black) and upper and lower quartile (gray), *p ≤ 0,05, **p ≤ 0,01, ***p ≤
892 0,001, ****p ≤ 0,0001.
893
894 **Figure 3: DNA damage leads to an activation of the mTORC1 pathway in podocytes *in vivo*.**
895 A: Representative immunofluorescence staining of SNP, pS6RP and DAPI in sections of 9-week-old *Ercc1*
896 ctrl and pko kidneys with quantification of SNP and pS6RP double positive cells per glomerulus and per
897 total SNP positive cells, scalebar indicating 10 μm (n=5, 10 glomeruli per sample).

898 B: Representative Periodic Acid Schiff (PAS) staining of end-of-life *Ercc1* -/delta mice treated with 14 mg
899 rapamycin per kg food from 8 weeks of age and glomerulosclerosis-assessment of all glomeruli depicted as
900 parts of a whole and scatter plot (n = 8, 50 glomeruli per sample), scalebar indicating 50 μm.
901 C: Representative Periodic Acid Schiff (PAS) staining of *Ercc1* pko mice treated with vehicle (*Ercc1* pko) or
902 2mg rapamycin per kg bodyweight (*Ercc1* pko Rapa) from 6 weeks of age and glomerulosclerosis-
903 assessment of all glomeruli depicted as parts of a whole and scatter plot (n ≥ 9, 50 glomeruli per sample),
904 scalebar indicating 50 μm.
905 D: Representative immunofluorescence staining of synaptopodin (SNP, gray), DNA damage marker γH2A.X
906 (green) and nuclear marker Draq5 (red) in sections of 4-week-old *Tsc1* ctrl and pko kidneys, with
907 quantification of γH2A.X foci per podocyte nucleus and nuclear area of *Ercc1* ctrl and pko kidneys, yellow
908 dotted line indicating nuclear border (n=5, 10 glomeruli per sample, 5 podocytes per glomerulus), scalebar
909 indicating 2 μm.
910 E: Schematic overview depicting the potential interplay between defective DNA damage repair and
911 increased mTORC1 signaling. In *Ercc1* pko mice, accumulation of DNA damage triggers mTORC1
912 signaling. In *Tsc1* pko mice, hyperactive mTORC1 signaling also leads to increased DNA damage foci.
913 All violin plots indicate median (black) and upper and lower quartile (gray), scatterplots indicate mean plus
914 95% confidence interval, *p ≤ 0,05, **p ≤ 0,01, ***p ≤ 0,001, ****p ≤ 0,0001.
915
916 **Figure 4: DNA damage leads to an activation of the mTORC1 pathway in podocytes through a DNA-**
917 **PK-dependent mechanism.**
918 A: Schematic *in vitro* protocol for the induction of DNA damage.
919 B: Representative immunoblot images for DNA damage marker γH2A.X and loading control protein beta-
920 tubulin of immortalized murine podocyte lysates (n=3).
921 C: Representative immunofluorescence images for tumor suppressor p53 and nuclear marker DAPI in
922 immortalized murine podocytes (n=3).
923 D: Representative immunoblot images for mTORC1 target phospho-S6 ribosomal protein (pS6RP), S6RP
924 and loading control protein alpha-actin of immortalized murine podocyte lysates (n=3).
925 All cells imaged or lysed after treatment with mitomycin C (MMC) or ultraviolet C (UV-C) irradiation ± 10
926 ng/ml rapamycin or serum starvation (SS), n ≥ 4.
927 E: Representative immunoblot images for mTORC1 target phospho-S6 ribosomal protein (pS6RP), S6RP
928 and loading control protein alpha-actin of immortalized murine podocyte lysates (n=3 MMC; n=6 UV-C).
929 All cells imaged or lysed after treatment with mitomycin C (MMC) or ultraviolet C (UV-C) irradiation ± ATM
930 inhibitor KU60019 or DNA-PK inhibitor nedisertib.
931
932 **Figure 5: Podocytes accumulate DNA damage with aging and during human FSGS.**
933 A: Representative immunofluorescence staining of SNP, γH2A.X, and Draq5 in sections of murine young
934 and aged wildtype kidneys with quantification of γH2A.X foci per podocyte nuclear area, scalebar indicating
935 2 μm, n=4, 5 glomeruli per sample, 5 podocytes per glomerulus.
936 B: Representative immunofluorescence staining of SNP, γH2A.X, and Draq5 in sections of human young
937 and old tumor nephrectomy kidneys with quantification of γH2A.X foci per podocyte nuclear area and per
938 podocyte nucleus, scalebar indicating 5 μm, n≥4, 5 glomeruli per sample, 5 podocytes per glomerulus.
939 C: UMAP of single nucleus sequencing data set (50) depicting the identification of 24 different cell types in
940 analysed control, minimal change disease, and focal segmental glomerulosclerosis biopsies. FIB/Immue:
941 Fibroblasts/Immune cells, C-TAL/MD: Thick ascending limb of loop of Henle, PT-1-6: proximal tubular cells,
942 DTL: descending thin limb, PC-CNT: Connecting Tubule, EC-PT: Endothelial Cell, FIB: Fibroblast, DCT:
943 Distal convoluted tubule, IC-A: Intercalated cell A, vSMC/MC-1: vascular smooth muscle cell/Muscle cell1,
944 TAL: Thick ascending limb of loop of Henle, T_Cell: T cells, MAC/MON: Macrophage/Monocyte, MD:

Medullary cell, vSMC/MC-2: vascular smooth muscle cell/Muscle cell2, PEC: Parietal epithelial cell, GC-EC: Glomerular endothelial cell, IC-B: Intercalated cell B, POD: Podocyte..
D: Bubble plot indicating the differences in DNA repair and mTORC1 target gene expression in podocytes between living donor (LD) kidney samples, Minimal change disease (MCD) and FSGS biopsies obtained through single nucleus sequencing (50). Bubble size indicating percentage of podocytes expressing the target gene, bubble colour indicating expression level, grey line indicating the split between DNA repair and mTORC1 target genes.
E: Selected scatterplots of ERCC1 and ERCC4 expression data of single podocytes obtained from living donor (LD), Minimal change disease (MCD), and FSGS biopsies.
F: Selected scatterplots of RNA polymerase 1-3 subunit POLR2K and RNA polymerase 2 subunit POLR2J of single podocytes obtained from living donor (LD), Minimal change disease (MCD), and FSGS biopsies.
G: Representative immunofluorescence staining of synaptopodin (SNP), γH2A.X, and Draq5 in sections of human MCD and FSGS biopsies, yellow dotted line indicating nuclear border, scalebar indicating 2 μm with quantification of γH2A.X foci per podocyte nuclear area and per podocyte nucleus in human MCD and FSGS biopsies (n=4, 4 glomeruli per sample, 5 podocytes per glomerulus).
All violin plots indicate median (black) and upper and lower quartile (gray), *p ≤ 0,05, ***p ≤ 0,001, ****p ≤ 0,0001.

Supplementary Information:

Fig S1:

GSEA of gene classes according to transcript length. Shown are the analyses for the shortest 5 % (top left), shortest 1 % (top right), longest 5% (bottom left), and longest 1% (bottom right) of genes. The bottom of each panel shows the log2 fold changes of the microarray data in a ranked order. The top panels show the running enrichment score as an orange line. The smallest 1% (normalized enrichment score (NES) of 2.01) and 5% (NES of 1.37) of genes are significantly more enriched in the upregulated genes, while the longest 1% (NES of -1.69) and 5% (NES of -1.42) of genes are significantly enriched in the downregulated genes in the comparison *Ercc1* -/delta 14 weeks vs. WT 14 weeks.

Figure S2:

A: Breeding scheme for homozygous and heterozygous podocyte-specific *Ercc1* pko mice.
B: Representative Coomassie blue staining of *Ercc1* ctrl and wt/pko (het) urine at 36 weeks of age; bovine serum albumin (BSA) was loaded as reference.
C: Representative Periodic Acid Schiff (PAS) staining of *Ercc1* wt/pko (het) kidney at 72 weeks of age, scalebar: 100 μm.

Figure S3:

A: Breeding and induction scheme for homozygous inducible podocyte-specific *Ercc1* ko mice (ipko).
B: Kaplan-Meyer curve depicting survival of *Ercc1* ctrl and ipko mice (Mantel-Cox test).
C: Representative Coomassie blue staining of *Ercc1* ctrl and ipko urine 18 weeks after induction with tamoxifen; bovine serum albumin (BSA) was loaded as reference (n=6).
D: Representative Periodic Acid Schiff (PAS) staining of *Ercc1* ctrl and ipko mice 25 weeks after induction with tamoxifen (n=6).

989 *p ≤ 0,05, scalebar: 100μm.
990

991 **Figure S4:**
992 A: Quantification of nephrin positive area in μm^2 of *Ercc1* ctrl and pko kidneys at 7, 9, 11, and 13 weeks of
993 age, n=4, 10 glomeruli per sample.
994 B: Quantification of glomerular volume of 9-week-old *Ercc1* ctrl and pko kidneys, n = 5, 10 glomeruli per
995 sample.
996 C: Quantification of WT+ nuclei per glomerulus of *Ercc1* ctrl and pko kidneys at 9 and 11 weeks of age, n =
997 4, ≥50 glomeruli per group.
998 D: Quantification of podocyte nuclear area of 9-week-old *Ercc1* ctrl and pko kidneys, n = 5, 10 glomeruli per
999 sample, 5 podocytes per glomerulus.
1000 E: Quantification of γH2A.X foci area per podocyte nucleus of 9-week-old *Ercc1* ctrl and pko kidneys, n = 5,
1001 10 glomeruli per sample, 5 podocytes per glomerulus.
1002 F: Quantification of γH2A.X foci area per podocyte nuclear area of 9-week-old *Ercc1* ctrl and pko kidneys,
1003 n = 5, 10 glomeruli per sample, 5 podocytes per glomerulus.
1004 All violin plots indicate median (black) and upper and lower quartile (gray), **p ≤ 0,01, ***p ≤ 0,001, ****p ≤
1005 0,0001.
1006

1007 **Figure S5:**
1008 A: urinary albumin/creatinine analysis; B: serum creatinine analysis; C: serum urea analysis and weight
1009 analysis (D: female; E: male) of *Ercc1* pko mice treated with vehicle (Ercc1pko) or rapamycin (Ercc1pko
1010 Rapa).
1011 F: Representative image of rapamycin and vehicle treated *Ercc1* pko mice at 13 weeks of age depicting
1012 edema in the vehicle treated animal.
1013 All scatterplots indicate mean plus 95% confidence interval, **p ≤ 0,01, ****p ≤ 0,0001, scalebars: 50μm.
1014

1015 **Figure S6:**
1016 A: Representative immunohistochemistry staining of pS6RP in sections of murine young and aged wildtype
1017 kidneys with quantification of pS6RP-positive cells per glomerulus, scalebar indicating 25 μm, n = 11, 50
1018 glomeruli per sample.
1019 B: Representative immunofluorescence staining of SNP, pS6RP, and DAPI in sections of young and old
1020 human tumor nephrectomy kidneys with quantification of SNP and pS6RP double positive cells per
1021 glomerulus and per total SNP positive cells, scalebar indicating 10 μm, n=≥4, 10 glomeruli per sample.
1022 Scatterplot depicting mean and 95% confidence interval, all violin plots indicating median (black) and upper
1023 and lower quartile (gray), ****p ≤ 0,0001.
1024

1025 **Figure S7:**
1026 Expression profile of 118 hallmark DNA repair genes in MCD, FSGS, IgA nephropathy (IgA), membranous
1027 nephropathy (MGN), diabetic nephropathy (DN), and hypertension (HT) glomeruli compared to controls
1028 depicted as parts of whole and single genes in heatmaps. Genes ranked by their protein abundance
1029 (Intensity-based absolute quantification - IBAQ) in murine podocyte proteome analysis (41).
1030

1031 **Figure S8:**
1032 Scatterplots of ERCC family and RNA polymerase subunit expression data of single podocytes obtained
1033 from living donor (LD), Minimal change disease (MCD), and FSGS biopsies.
1034

1035 **Table S1: Gene expression analysis of ERCB for Hallmark DNA Repair and Nucleotide Excision**
1036 **Repair Genes**
1037
1038 **Table S2: Clinical characteristics of FSGS patients**
1039
1040 **Table S3: eQTL analysis of DNA repair genes in FSGS patients**
1041 Ensg: ensemble gene ID; FDR: false discovery rate, PIP: posterior inclusion probability, AF:
1042 allele frequency, beta: expression difference to reference allele
1043
1044 **Table S4: Full eQTL analysis of DNA repair genes in FSGS patients**
1045
1046

figure 1:

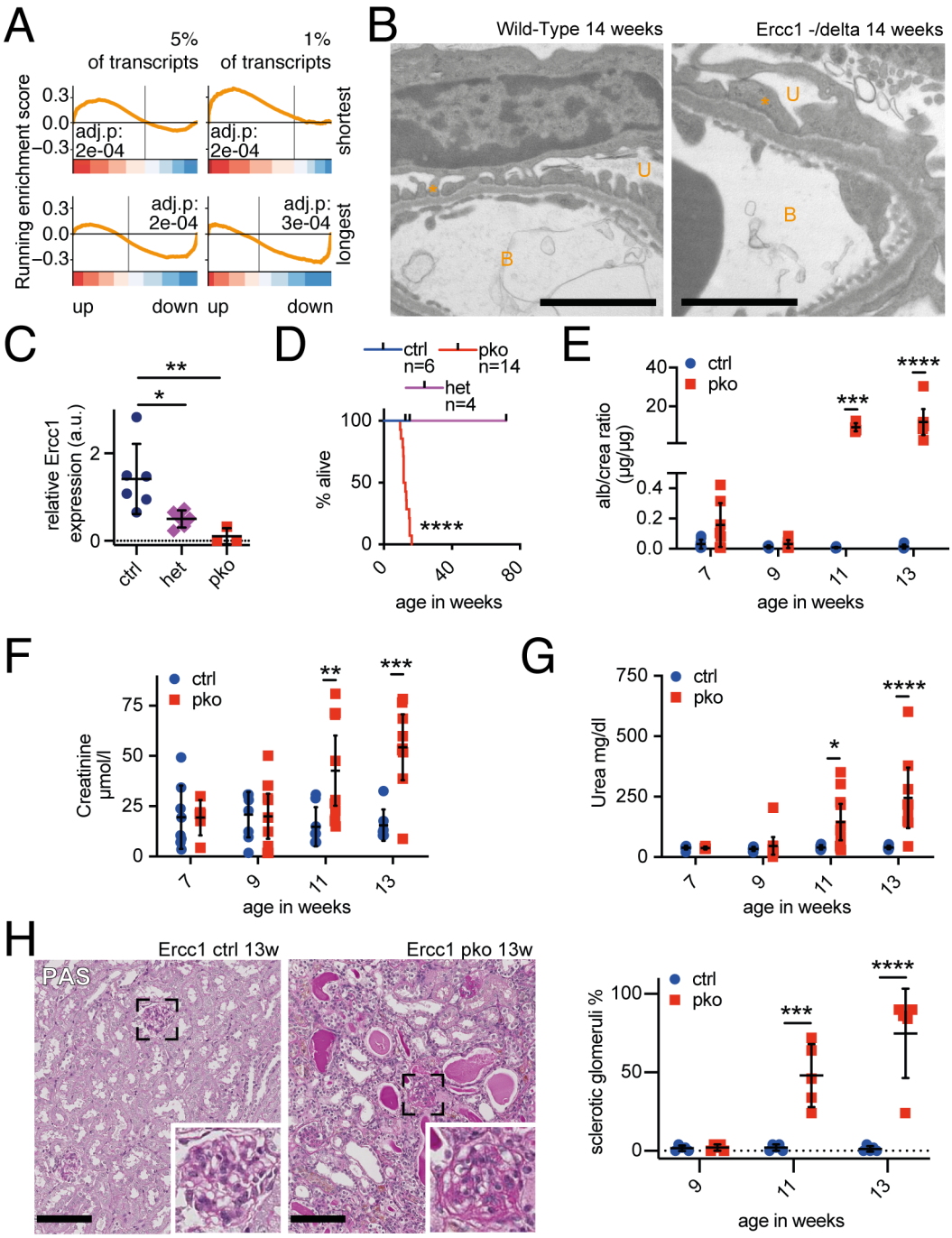

Figure 1: The podocyte-specific constitutive ko of Ercc1 causes glomerulosclerosis.
A: GSEA of gene classes according to transcript length. Shown are the analyses for the shortest 5 % (top left), shortest 1 % (top right), longest 5% (bottom left), and longest 1% (bottom right) of genes. The bottom color-coded panel shows the log2 fold changes of the microarray data in a ranked order. The top panels show the running enrichment score as an orange line. The smallest 1% (normalized enrichment score (NES) of 2.01) and 5% (NES of 1.37) of genes are significantly enriched in the upregulated genes, while the longest 1% (NES of -1.69) and 5% (NES of -1.42) of genes are significantly enriched in the downregulated genes in the comparison Ercc1 -/delta 14 weeks vs. WT 14 weeks.
B: Representative electron microscopy image of 14-week-old wild-type (WT) and Ercc1 -/delta glomerular filtration barrier, scalebar indicating 2 μm, B: blood side – intracapillary space, U: urinary side – bowman's space, asterisk indicating podocyte foot process (n=4).
C: qPCR analysis for Ercc1 in FACS-sorted podocytes of Ercc1 ctrl, wt/pko (het) or pko mice. Delta-Delta-CT values expressed as scatterplots depicting mean plus 95% confidence interval.
D: Kaplan-Meyer curve depicting survival of Ercc1 ctrl, wt/pko (het) and pko mice (Mantel-Cox test).
E: urinary albumin/creatinine analysis; F: serum creatinine analysis; G: serum urea analysis of Ercc1 ctrl and pko mice.
H: Representative Periodic Acid Schiff (PAS) staining of 13-week-old Ercc1 ctrl and pko mice and quantification of sclerotic glomeruli, scalebars: 100 μm, n = 5, 50 glomeruli per sample.
Scatterplots indicate mean plus 95% confidence interval, *p ≤ 0,05, **p ≤ 0,01, ***p ≤ 0,001, ****p ≤ 0,0001.

figure 2:

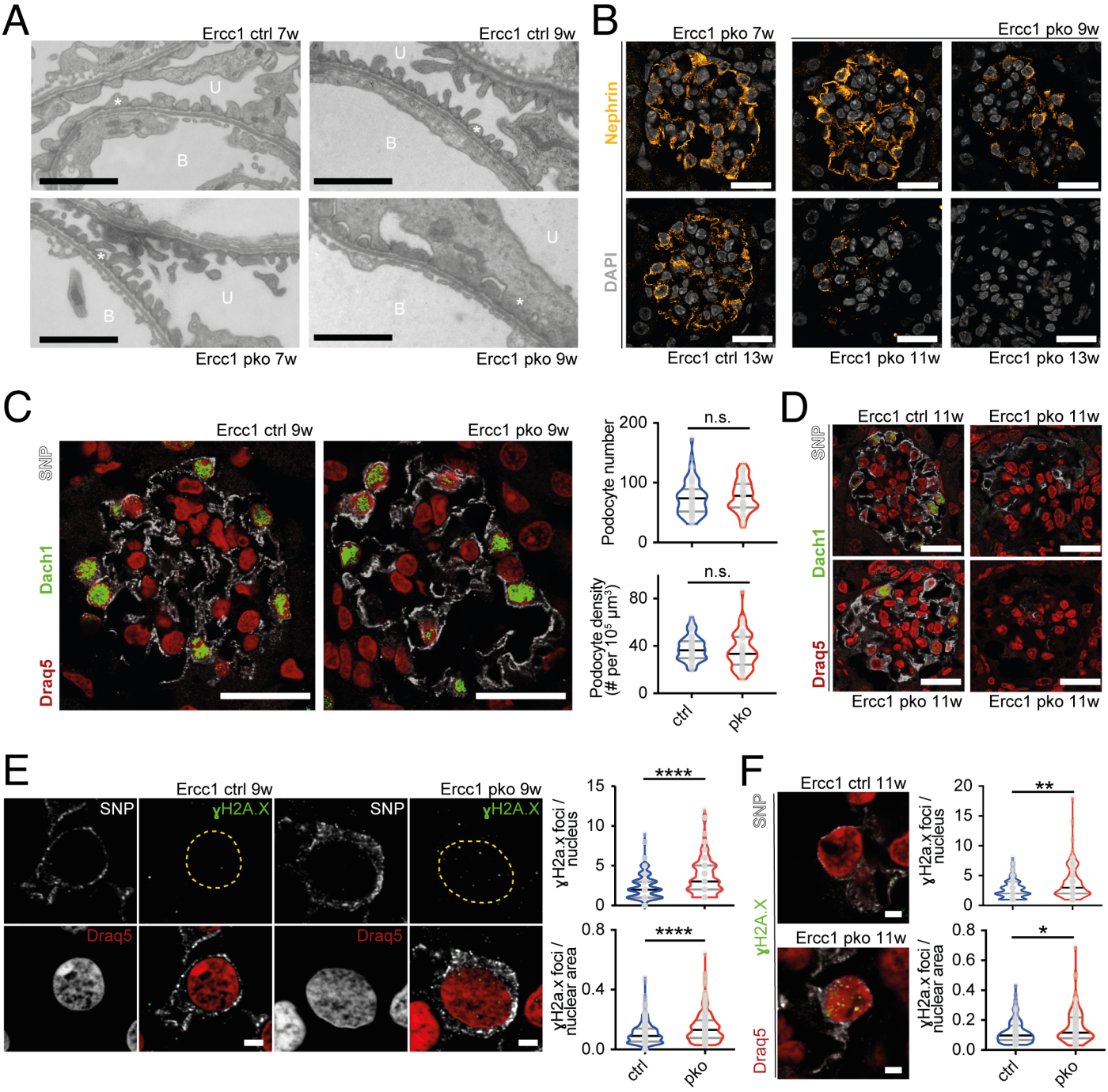

Figure 2: The podocyte-specific constitutive ko of Ercc1 leads to foot process effacement and podocyte loss accompanied by accumulation of DNA damage.
A: Representative electron microscopy image of 7- and 9-week-old Ercc1 ctrl and pko slit diaphragms, scalebar indicating 2 μm, B: blood side – intracapillary space, U: urinary side – Bowman's space, asterisk indicating podocyte foot process (n=3).
B: Representative immunofluorescence staining of slit diaphragm protein nephrin (yellow) with nuclear marker DAPI (grey) of Ercc1 ctrl at 13 weeks of age and pko kidneys at 7, 9, 11, and 13 weeks of age, scalebar indicating 2 μm (n=5).
C: Representative immunofluorescence staining of podocyte proteins synaptopodin (SNP, gray), Dachshund homolog 1 (Dach1, green) (43) and far-red fluorescent DNA dye Draq5 (red) as a nuclear marker in sections of 9-week-old Ercc1 ctrl and pko kidneys, with quantification of podocyte number and density of Ercc1 ctrl and pko kidneys, scalebar indicating 10 μm (n=5).
D: Corresponding staining of podocyte proteins synaptopodin (gray), Dachshund homolog 1 (Dach1, green) (43) and far-red fluorescent DNA dye Draq5 (red) as a nuclear marker in paraffin-embedded sections of 11-week-old Ercc1 ctrl and pko kidneys, scalebar indicating 10 μm (n=5).
E: Representative immunofluorescence staining of synaptopodin (SNP, gray), DNA damage marker γH2A.X (green) and nuclear marker Draq5 (red) in sections of 9-week-old Ercc1 ctrl and pko kidneys, with quantification of γH2A.X foci per podocyte nucleus and nuclear area of Ercc1 ctrl and pko kidneys, scalebar indicating 2 μm, yellow dotted line indicating nuclear border, n=5, 10 glomeruli per sample, 5 podocytes per glomerulus.
F: Representative immunofluorescence staining of synaptopodin (SNP, gray), DNA damage marker γH2A.X (green) and nuclear marker Draq5 (red) in sections of 11-week-old Ercc1 ctrl and pko kidneys, with quantification of γH2A.X foci per podocyte nucleus and nuclear area of Ercc1 ctrl and pko kidneys, scalebar indicating 2 μm, n=5, 10 glomeruli per sample, 5 podocytes per glomerulus.
All violin plots indicate median (black) and upper and lower quartile (gray), *p ≤ 0,05, **p ≤ 0,01, ***p ≤ 0,001, ****p ≤ 0,0001.

figure 3:

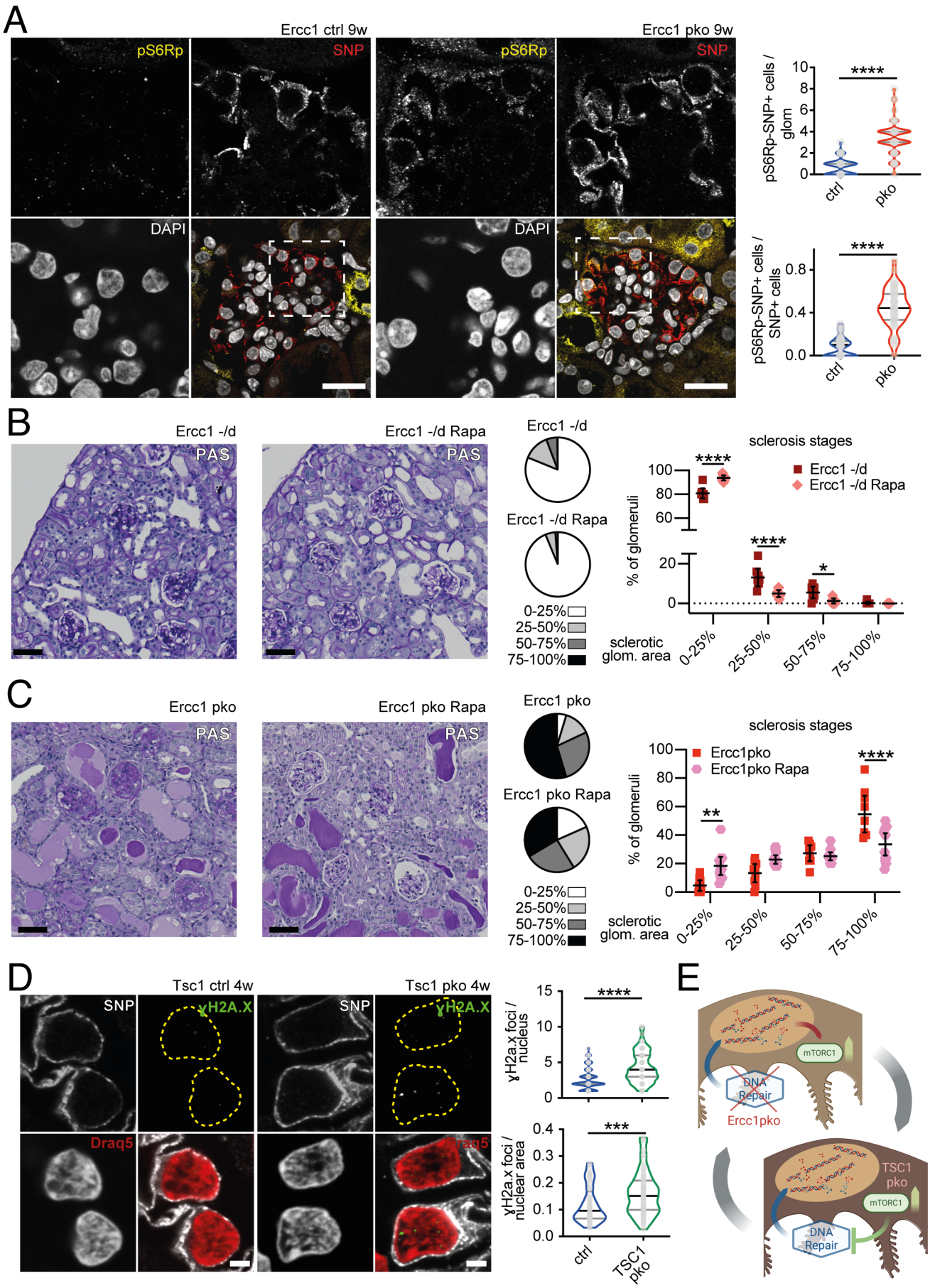

Figure 3: DNA damage leads to an activation of the mTORC1 pathway in podocytes in vivo.
A: Representative immunofluorescence staining of SNP, pS6RP and DAPI in sections of 9-week-old Ercc1 ctrl and pko kidneys with quantification of SNP and pS6RP double positive cells per glomerulus and per total SNP positive cells, scalebar indicating 10 μm (n=5, 10 glomeruli per sample).
B: Representative Periodic Acid Schiff (PAS) staining of end-of-life Ercc1 -/delta mice treated with 14 mg rapamycin per kg food from 8 weeks of age and glomerulosclerosis-assessment of all glomeruli depicted as parts of a whole and scatter plot (n = 8, 50 glomeruli per sample), scalebar indicating 50 μm.
C: Representative Periodic Acid Schiff (PAS) staining of Ercc1 pko mice treated with vehicle (Ercc1 pko) or rapamycin (Ercc1 pko Rapa) from 6 weeks of age and glomerulosclerosis-assessment of all glomeruli depicted as parts of a whole and scatter plot (n ≥ 9, 50 glomeruli per sample), scalebar indicating 50 μm.
D: Representative immunofluorescence staining of synaptopodin (SNP, gray), DNA damage marker γH2A.X (green) and nuclear marker Draq5 (red) in sections of 4-week-old Tsc1 ctrl and pko kidneys, with quantification of γH2A.X foci per podocyte nucleus and nuclear area of Ercc1 ctrl and pko kidneys, yellow dotted line indicating nuclear border (n=5, 10 glomeruli per sample, 5 podocytes per glomerulus), scalebar indicating 2 μm.
E: Schematic overview depicting the potential interplay between defective DNA damage repair and increased mTORC1 signaling. In Ercc1 pko mice, accumulation of DNA damage triggers mTORC1 signaling. In Tsc1 pko mice, hyperactive mTORC1 signaling also leads to increased DNA damage foci.
All violin plots indicate median (black) and upper and lower quartile (gray), scatterplots indicate mean plus 95% confidence interval, *p ≤ 0,05, **p ≤ 0,01, ***p ≤ 0,001, ****p ≤ 0,0001.

figure 4:

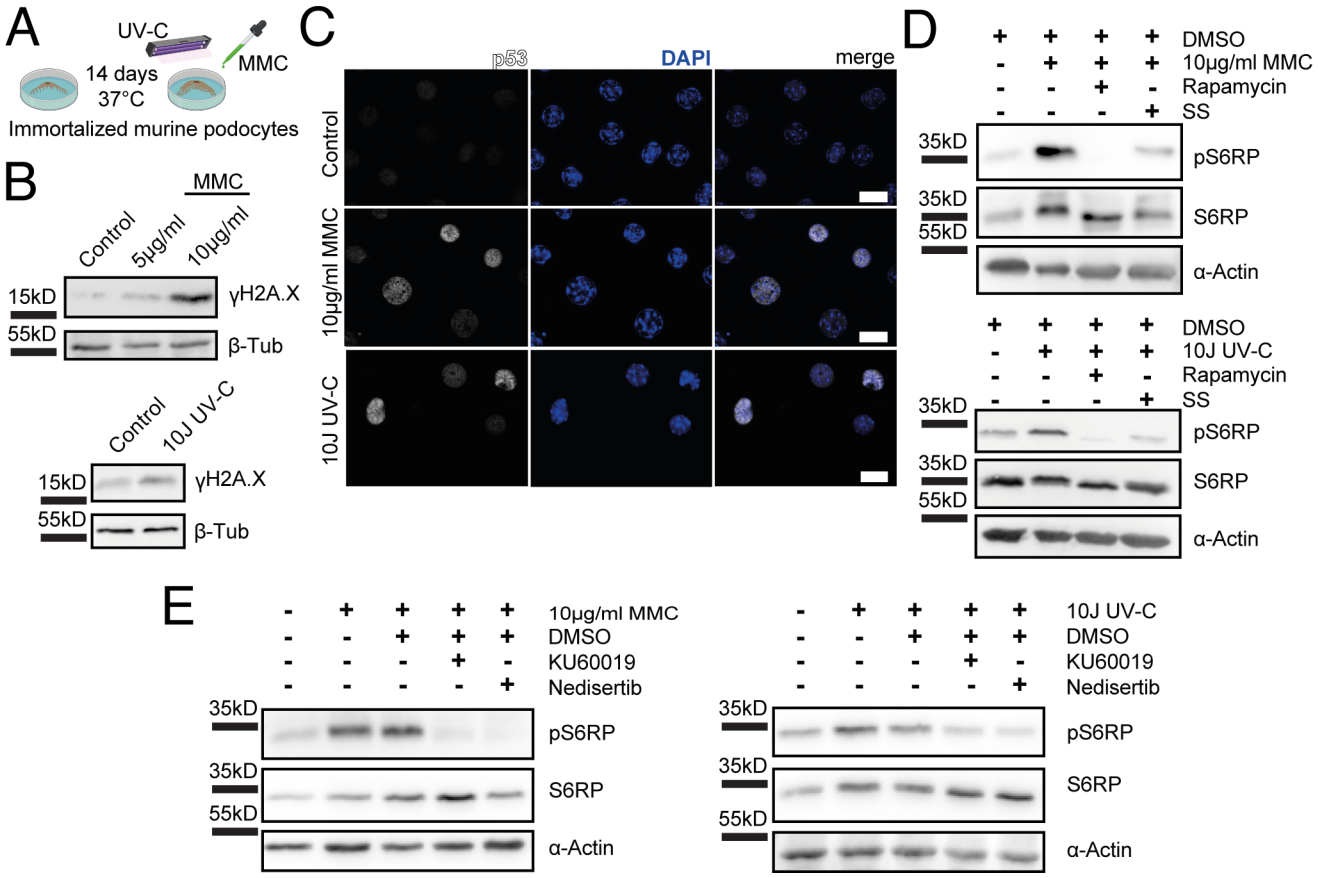

Figure 4: DNA damage leads to an activation of the mTORC1 pathway in podocytes through a DNA-PK-dependent mechanism.
A: Schematic in vitro protocol for the induction of DNA damage.
B: Representative immunoblot images for DNA damage marker γH2A.X and loading control protein beta-tubulin of immortalized murine podocyte lysates (n=3).
C: Representative immunofluorescence images for tumor suppressor p53 and nuclear marker DAPI in immortalized murine podocytes (n=3).
D: Representative immunoblot images for mTORC1 target phospho-S6 ribosomal protein (pS6RP), S6RP and loading control protein alpha-actin of immortalized murine podocyte lysates (n=3).
All cells imaged or lysed after treatment with mitomycin C (MMC) or ultraviolet C (UV-C) irradiation ± 10 ng/ml rapamycin or serum starvation (SS), n ≥ 4.
E: Representative immunoblot images for mTORC1 target phospho-S6 ribosomal protein (pS6RP), S6RP and loading control protein alpha-actin of immortalized murine podocyte lysates (n=3 MMC; n=6 UV-C).
All cells imaged or lysed after treatment with mitomycin C (MMC) or ultraviolet C (UV-C) irradiation ± ATM inhibitor KU60019 or DNA-PK inhibitor nedisertib.

figure 5:

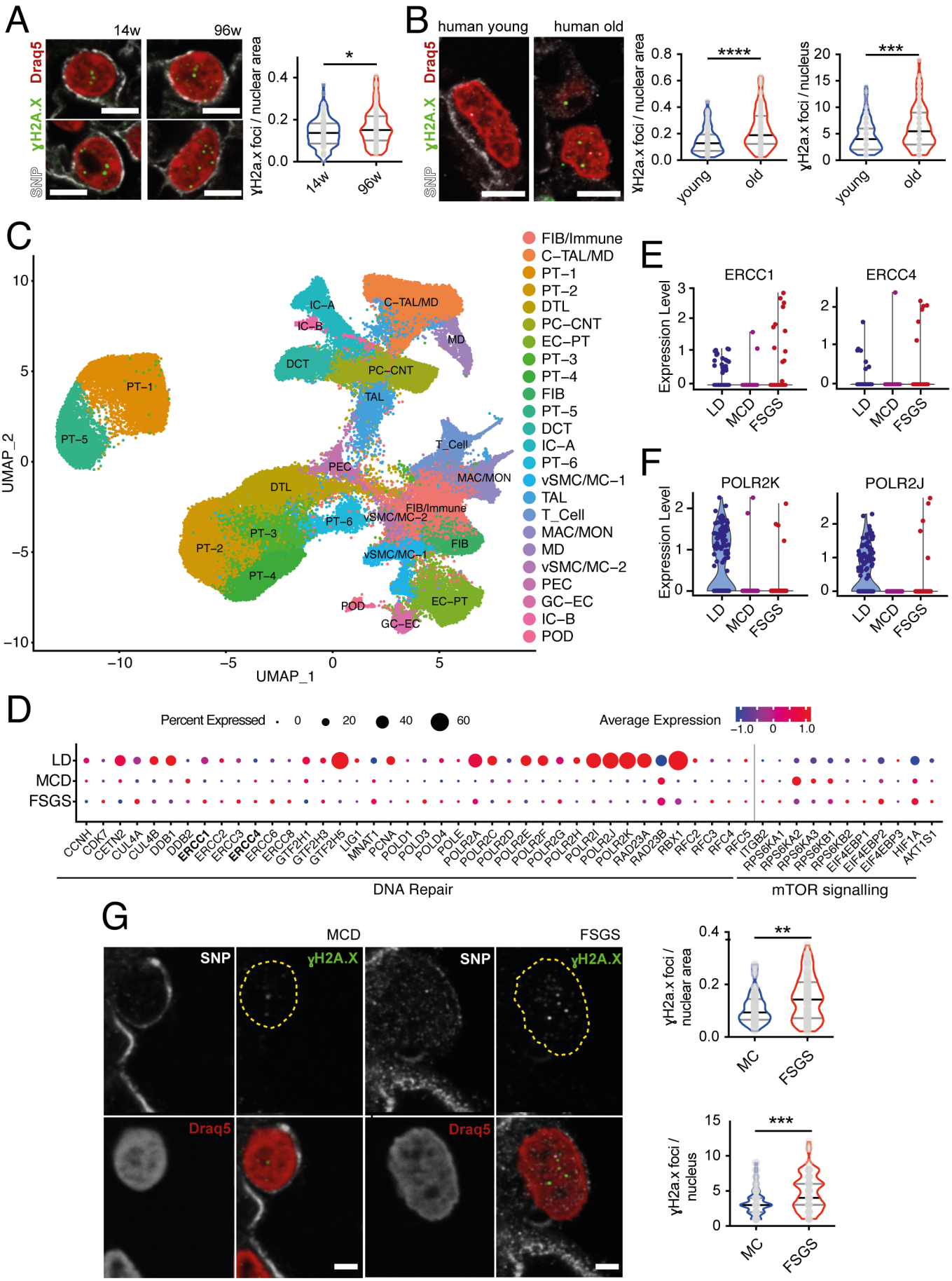

Figure 5: Podocytes accumulate DNA damage with aging and during human FSGS.
A: Representative immunofluorescence staining of SNP, γH2A.X, and Draq5 in sections of murine young and aged wildtype kidneys with quantification of γH2A.X foci per podocyte nuclear area, scalebar indicating 2 μm, n=4, 5 glomeruli per sample, 5 podocytes per glomerulus.
B: Representative immunofluorescence staining of SNP, γH2A.X, and Draq5 in sections of human young and old tumor nephrectomy kidneys with quantification of γH2A.X foci per podocyte nuclear area and per podocyte nucleus, scalebar indicating 5 μm, n≥4, 5 glomeruli per sample, 5 podocytes per glomerulus.
C: UMAP of single nucleus sequencing data set (50) depicting the identification of 24 different cell types in analysed control, minimal change disease and focal segmental glomerulosclerosis biopsies. FIB/Immue: Fibroblasts/Immune cells, C-TAL/MD: Thick ascending limb of loop of Henle, PT-1-6: proximal tubular cells, DTL: descending thin limb, PC-CNT: Connecting Tubule, EC-PT: Endothelial Cell, FIB: Fibroblast, DCT: Distal convoluted tubule, IC-A: Intercalated cell A, vSMC/MC-1: vascular smooth muscle cell/Muscle cell1, TAL: Thick ascending limb of loop of Henle, T_Cell: T cells, MAC/MON: Macrophage/Monocyte, MD: Medullary cell, vSMC/MC-2: vascular smooth muscle cell/Muscle cell2, PEC: Parietal epithelial cell, GC-EC: Glomerular endothelial cell, IC-B: Intercalated cell B, POD: Podocyte..
D: Bubble plot indicating the differences in DNA repair and mTORC1 target gene expression in podocytes between living donor (LD) kidney samples, Minimal change disease (MCD) and FSGS biopsies obtained through single nucleus sequencing (50). Bubble size indicating percentage of podocytes expressing the target gene, bubble colour indicating expression level, grey line indicating the split between DNA repair and mTORC1 target genes.
E: Selected scatterplots of ERCC1 and ERCC4 expression data of single podocytes obtained from living donor (LD), Minimal change disease (MCD), and FSGS biopsies.
F: Selected scatterplots of RNA polymerase 1-3 subunit POLR2K and RNA polymerase 2 subunit POLR2J of single podocytes obtained from living donor (LD), Minimal change disease (MCD), and FSGS biopsies.
G: Representative immunofluorescence staining of synaptopodin (SNP), γH2A.X, and Draq5 in sections of human MCD and FSGS biopsies, yellow dotted line indicating nuclear border, scalebar indicating 2 μm with quantification of γH2A.X foci per podocyte nuclear area and per podocyte nucleus in human MCD and FSGS biopsies (n=4, 4 glomeruli per sample, 5 podocytes per glomerulus).
All violin plots indicate median (black) and upper and lower quartile (gray), *p ≤ 0,05, ***p ≤ 0,001, ****p ≤ 0,0001.

figure S1:

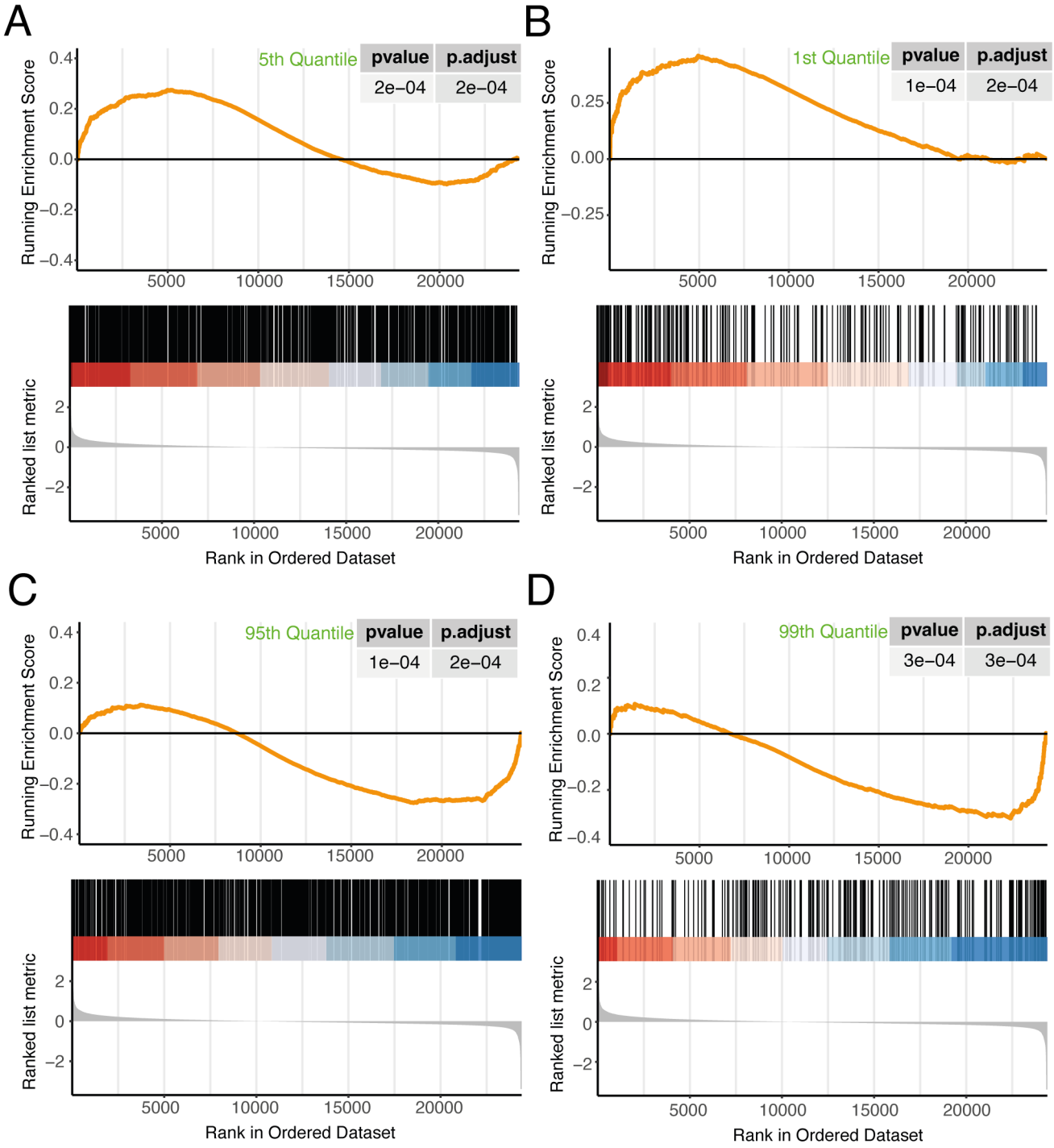

Fig S1:
GSEA of gene classes according to transcript length. Shown are the analyses for the shortest 5 % (top left), shortest 1 % (top right), longest 5% (bottom left), and longest 1% (bottom right) of genes. The bottom of each panel shows the log2 fold changes of the microarray data in a ranked order. The top panels show the running enrichment score as an orange line. The smallest 1% (normalized enrichment score (NES) of 2.01) and 5% (NES of 1.37) of genes are significantly more enriched in the upregulated genes, while the longest 1% (NES of -1.69) and 5% (NES of -1.42) of genes are significantly enriched in the downregulated genes in the comparison Ercc1 -/delta 14 weeks vs. WT 14 weeks.

figure S2:

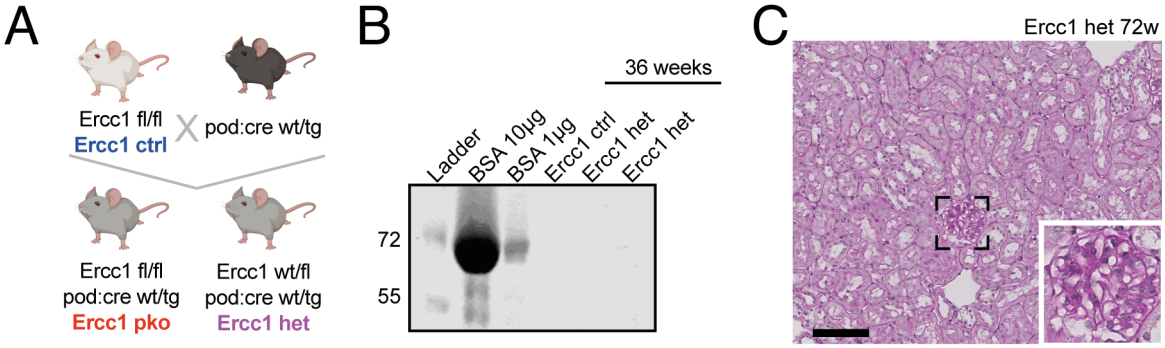

Figure S2:
A: Breeding scheme for homozygous and heterozygous podocyte-specific Ercc1 pko mice.
B: Representative Coomassie blue staining of Ercc1 ctrl and wt/pko (het) urine at 36 weeks of age; bovine serum albumin (BSA) was loaded as reference.
C: Representative Periodic Acid Schiff (PAS) staining of Ercc1 wt/pko (het) kidney at 72 weeks of age, scalebar: 100 μm.

figure S3:

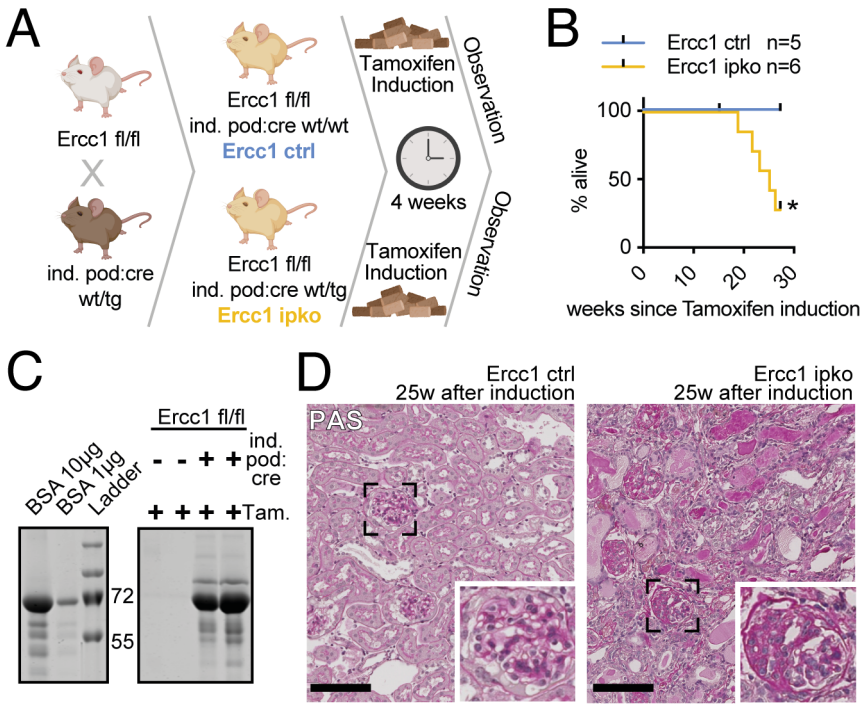

Figure S3:
A: Breeding and induction scheme for homozygous inducible podocyte-specific Ercc1 ko mice (ipko).
B: Kaplan-Meyer curve depicting survival of Ercc1 ctrl and ipko mice (Mantel-Cox test).
C: Representative Coomassie blue staining of Ercc1 ctrl and ipko urine 18 weeks after induction with tamoxifen; bovine serum albumin (BSA) was loaded as reference (n=6).
D: Representative Periodic Acid Schiff (PAS) staining of Ercc1 ctrl and ipko mice 25 weeks after induction with tamoxifen (n=6).*p ≤ 0,05, scalebar: 100μm.

figure S4:

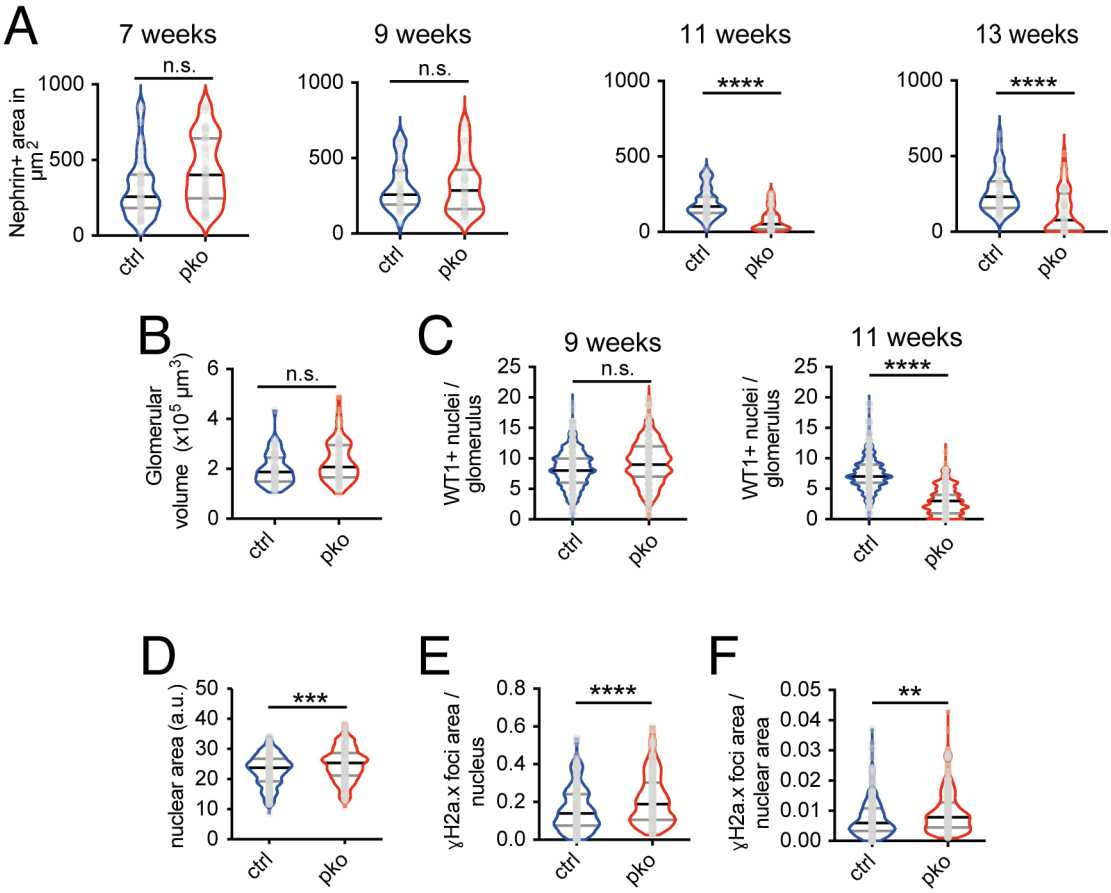

Figure S4:
A: Quantification of nephrin positive area in μm2 of Ercc1 ctrl and pko kidneys at 7, 9, 11, and 13 weeks of age, n=4, 10 glomeruli per sample.
B: Quantification of glomerular volume of 9-week-old Ercc1 ctrl and pko kidneys, n = 5, 10 glomeruli per sample.
C: Quantification of WT+ nuclei per glomerulus of Ercc1 ctrl and pko kidneys at 9 and 11 weeks of age, n = 4, ≥50 glomeruli per group.
D: Quantification of podocyte nuclear area of 9-week-old Ercc1 ctrl and pko kidneys, n = 5, 10 glomeruli per sample, 5 podocytes per glomerulus.
E: Quantification of γH2A.X foci area per podocyte nucleus of 9-week-old Ercc1 ctrl and pko kidneys, n = 5, 10 glomeruli per sample, 5 podocytes per glomerulus.
F: Quantification of γH2A.X foci area per podocyte nuclear area of 9-week-old Ercc1 ctrl and pko kidneys, n = 5, 10 glomeruli per sample, 5 podocytes per glomerulus.
All violin plots indicate median (black) and upper and lower quartile (gray), **p ≤ 0,01, ***p ≤ 0,001, ****p ≤ 0,0001.

figure S5:

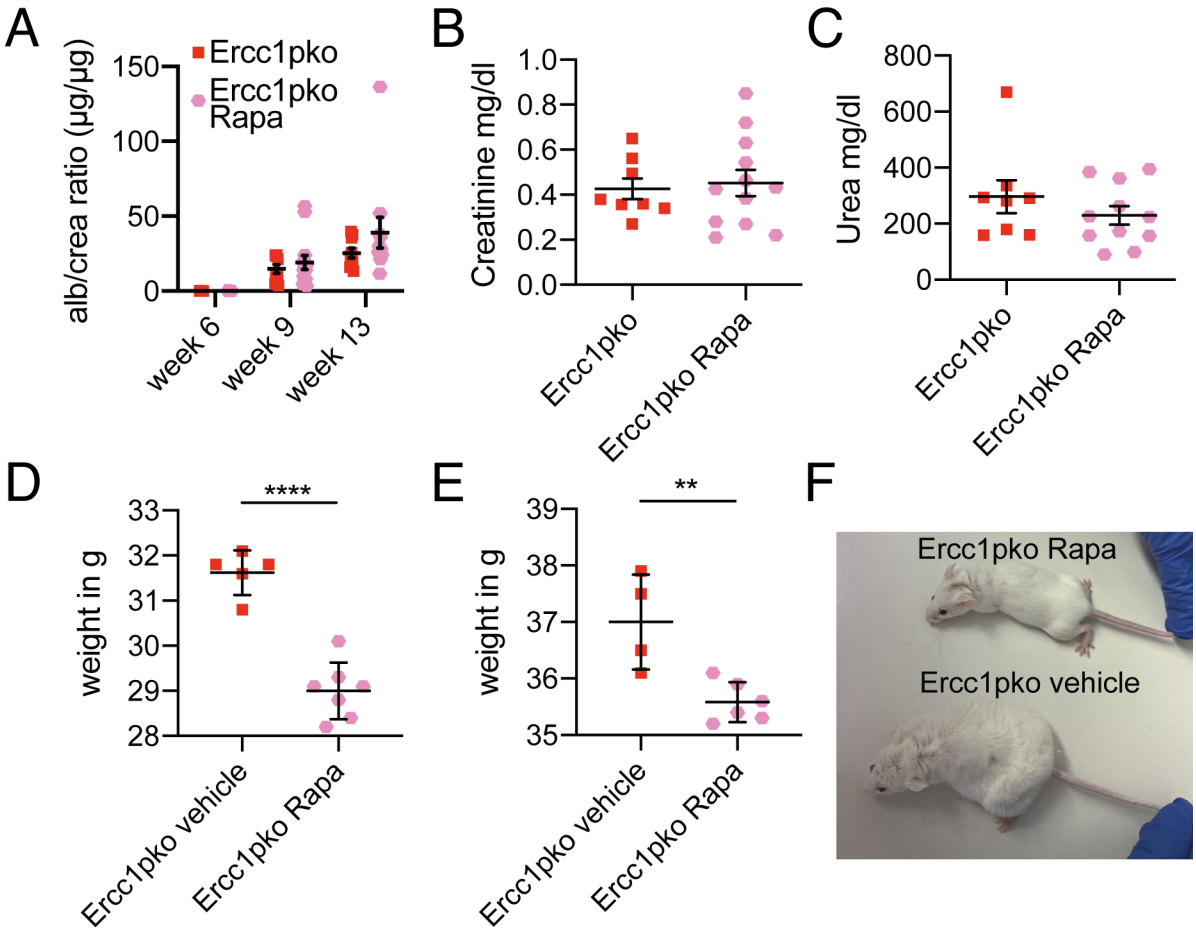

Figure S5:
A: urinary albumin/creatinine analysis; B: serum creatinine analysis; C: serum urea analysis and weight analysis (D: female; E: male) of Ercc1 pko mice treated with vehicle (Ercc1pko) or rapamycin (Ercc1pko Rapa).
F: Representative image of rapamycin and vehicle treated Ercc1 pko mice at 13 weeks of age depicting edema in the vehicle treated animal.
All scatterplots indicate mean plus 95% confidence interval, **$p \leq 0{,}01$, ****$p \leq 0{,}0001$, scalebars: 50μm.

figure S6:

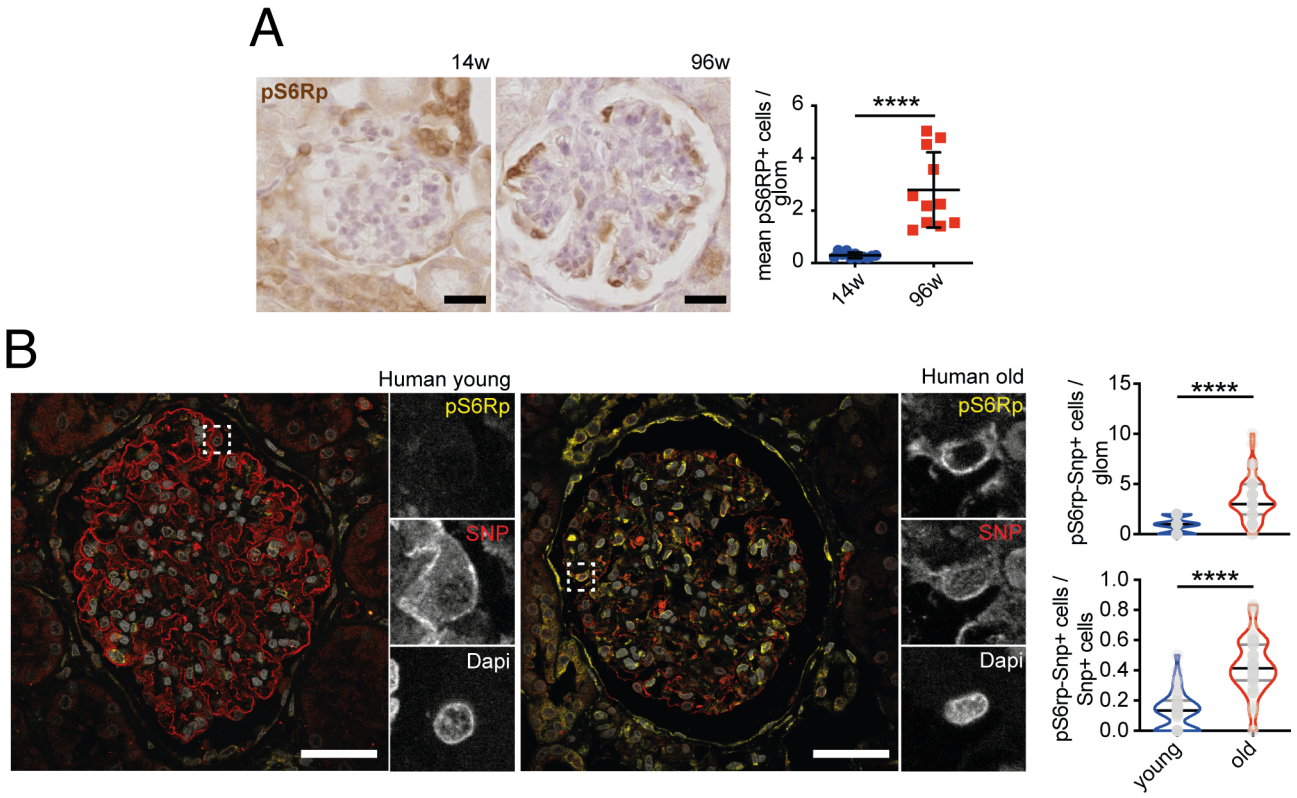

Figure S6:
A: Representative immunohistochemistry staining of pS6RP in sections of murine young and aged wildtype kidneys with quantification of pS6RP-positive cells per glomerulus, scalebar indicating 25 μm, n = 11, 50 glomeruli per sample.
B: Representative immunofluorescence staining of SNP, pS6RP, and DAPI in sections of young and old human tumor nephrectomy kidneys with quantification of SNP and pS6RP double positive cells per glomerulus and per total SNP positive cells, scalebar indicating 10 μm, n=≥4, 10 glomeruli per sample.
Scatterplot depicting mean and 95% confidence interval, all violin plots indicating median (black) and upper and lower quartile (gray), ****$p \leq 0{,}0001$.

figure S7:

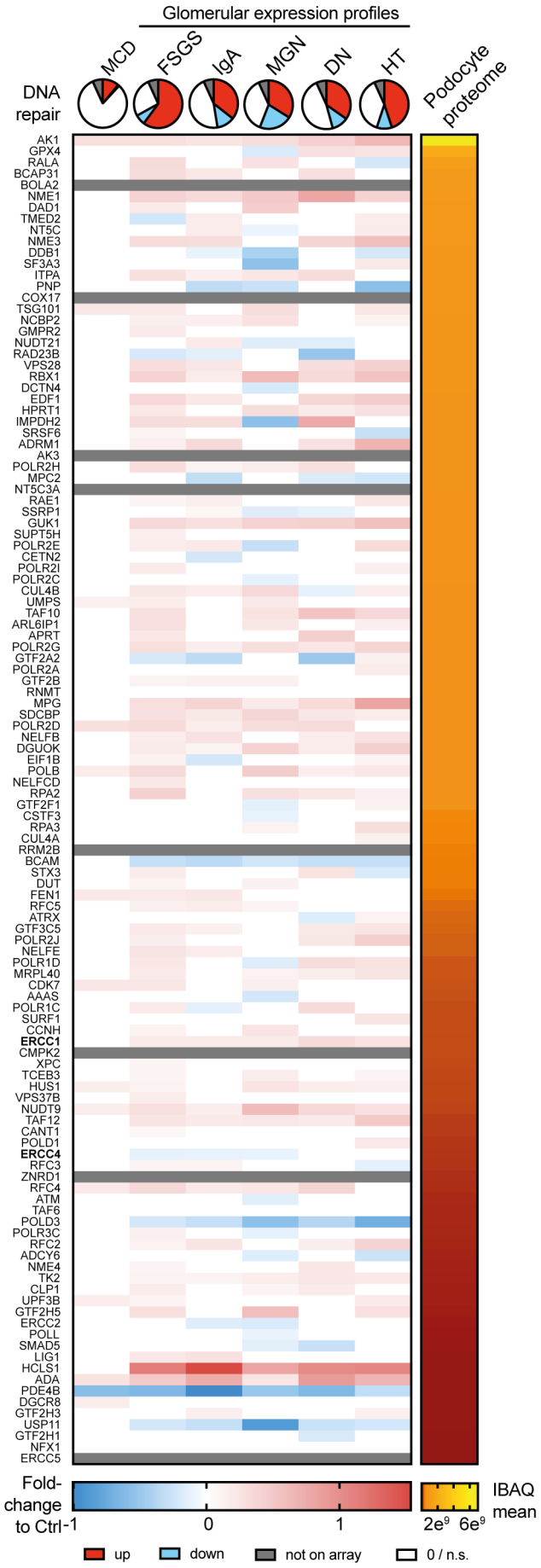

Figure S7:
Expression profile of 118 hallmark DNA repair genes in MCD, FSGS, IgA nephropathy (IgA), membranous nephropathy (MGN), diabetic nephropathy (DN), and hypertension (HT) glomeruli compared to controls depicted as parts of whole and single genes in heatmaps. Genes ranked by their protein abundance (Intensity-based absolute quantification - IBAQ) in murine podocyte proteome analysis (41).

figure S8:

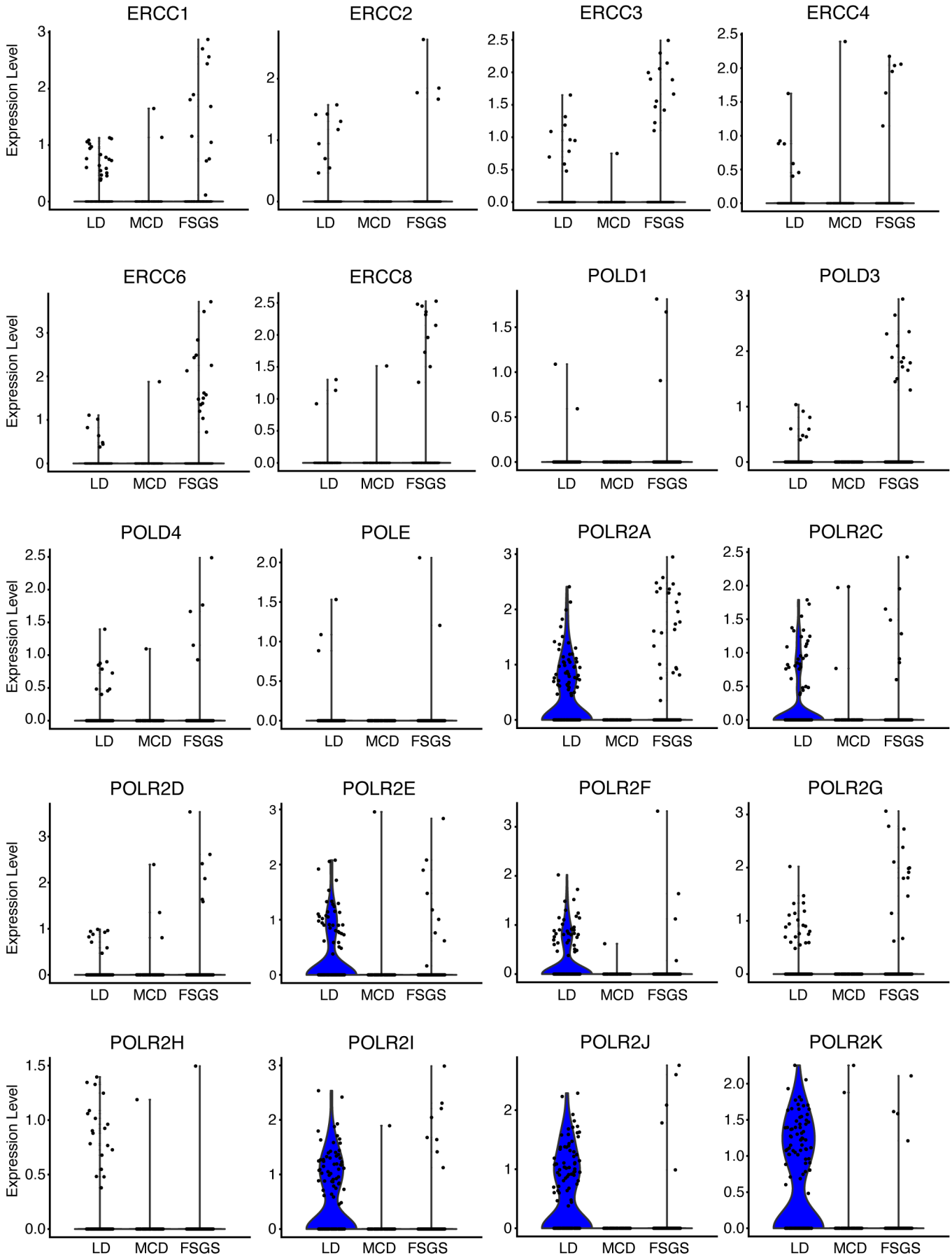

Figure S8:
Scatterplots of ERCC family and RNA polymerase subunit expression data of single podocytes obtained from living donor (LD), Minimal change disease (MCD), and FSGS biopsies.